New experimental techniques to study the adhesion to various solid surfaces of hydrate-relevant droplets and particles

Maren Andrea Dahl

Master thesis
University of Bergen

2010

Abstract

Hydrate plugging is a substantial problem in the oil and gas industry, both economically, environmentally and safety wise. Plugging may occur as a result of agglomeration of hydrate particles, deposition of hydrates on the pipeline wall, large hydrate particle loadings or a combination of the three. It would be an advantage to have the hydrates following the flow as a dispersion, instead of agglomerating and depositing onto the pipeline wall. This would prevent plugging. To do this, knowledge about the force between the hydrate and the pipeline material is required; A reduction in the brine-wall adhesive force is likely to indicate that the pipeline is less subjected to hydrate deposition.

In this work, the forces between hydrates or droplets of brine were investigated in various ways.

A stirred beaker setup was developed to easily investigate the effect of flow on hydrate deposition. The goal was to create a large data set of the flow rate required to detach a hydrate particle or droplet from various surfaces. To do this, a flow loop is often involved, but such a setup has been found difficult use for this purpose. A setup where the surface material could be easily changed was required and developed. The setup lived up to its expectations, but has to be refined.

The model used in these experiments was 15 wt% TBAB (Tetrabutylammonium bromide) in petroleum ether, and the solid surfaces investigated were glass, stainless steel, aluminum, brass and epoxy.

The static contact angles of brine of different surfaces were measured, and the results were used to calculate the adhesion energy. It was found that the epoxy surface is the only oil-wet surface, with a low adhesion energy. The brass surface is slightly water-wet, while glass, stainless steel and aluminum all have low contact angles, and corresponding high adhesion energy. This indicates that a water droplet will adhere less strongly to a epoxy surface, compared to the other surfaces in question.

Hydrates, in form of brine, hydrates grown on a surface and deposited hydrates, with and without acid in the oil phase, were tried detached from different surfaces, using the stirred beaker setup. A CFD model of the setup was used to determine the velocity of the fluid over the particle, and the drag force acting on the particle was calculated. It was found that the force needed to detach a water droplet and a deposited hydrate follows the trend of the calculated adhesion force between the solid surfaces and brine. It was also found that a hydrate grown on a surface adheres very strongly to the surface, while

a deposited dry particle adhere very poorly. A wet hydrate, on the other hand, detaches at the same Reynolds number as a droplet of brine, which indicates that capillary forces are the governing adhesion mechanism.

The stirred beaker setup was used to measure the dynamic contact angles of droplets of brine on various surface. An algorithm was used to calculated the force needed to dislodge the droplets. This force followed the trend of the calculated adhesion force between brine and the solid surfaces. There was reason to believe that the calculated forces were not correct, however, the fact that they followed the trend indicates that the setup can be used to make a trend. To calculated the exact forces, the algorithm has to be further developed.

Acknowledgments

Det praktiske arbeidet i forbindelse med denne oppgaven har vært utført ved Kjemisk Institutt ved Universitetet i Bergen. Oppgaven var i utgangspunktet en del av HYADES-prosjektet, som var et samarbeid mellom Sintef, Universitetet i Bergen, StatoilHydro og Chevron.

Jeg vil takke min veileder Alex C. Hoffmann for å alltid ha kontordøren åpen og være tilgjengelig for diskusjon og råd.

En stor takk også til Guro Aspenes for hennes grenseløse tålmodighet og uvurderlige hjelp, både i faglige spørsmål og i skriveprosessen.

Takk til Hyades-gruppen ved Sintef, spesielt Sylvi Høiland og Anna Borgund for å tålmodig svare på spørsmål og komme med forslag til eksperimentelt arbeid.

Takk til Boris Balakin for å lage CFD-modellen, forslag til forsøk og faglig hjelp, Franklin Krampa for hjelp med å installere STAR-CD, Egil Nodland for hjelp med infrarød analyse og Tanja Barth for å trekke tråder.

Takk til studieveileder Terje Finnekås for å gjære studiehverdagen så mye lettere.

Videre vil jeg takke Bergit Brattekås for støtte og tips i skriveprosessen og høyt verdsatte te-pauser. James R.Gasson og Djurdjica Corak for å alltid være vanvittig positive på mine vegne. Lesesal-vennene Vegard Eikill, Roy Dani Nyheim, Vidar Gjerde og Øystein Lee Aasen; det har vært veldig kjekt å dele kontor med dere!

Til slutt vil jeg takke familien og venner for all sttte, og spesielt Kenneth for at du er den du er. Jeg gleder meg til bli din kone!

Abbreviations

AA	Anti Agglomerants
ADSA-P	Axisymmetric Drop Shape Analysis - Profile
CFD	Computational Fluid Dynamics
KI	Kinetic Inhibitors
LDHI	Low-dosage Hydrate Inhibitors
MeOH	Methanol
MEG	Monoethylene Glycol
NICs	Natural Inhibiting Components
ppm	Parts per million
rpm	Revolutions Per Minute
TBAB	Tetra-n-butyl ammonium bromine

Symbols

α	Angle between the normal to the sphere at the bottom of the cap and the base plane
θ	Contact angle
θ_p	Contact angle between liquid and particle
θ_s	Slope of the probe's contour at the contact line
θ_{adv}	Advancing contact angle
θ_{rec}	Receding contact angle
γ_{AB}	Interfacial tension between A and B
γ_C	Surface tension of C
σ	Standard deviation
Δp	Pressure difference
$\Delta \rho$	Density difference
μ	Viscosity
ρ	Density
A	Representative area
c	Continuous phase
C	Celsius
C_D	Drag Coefficient
d	Diameter of particle/droplet
D_{pipe}	Diameter of pipeline
$D_{stirrer}$	Diameter of stirrer
F	Correction factor
F_A	Adhesion force
F_B	Buoyancy force
F_D	Drag force
$F_D is$	Dislodgement force
F_L	Lift forces
F_S	Force due to surface tension along the contact line
h	Height of spherical cap
l_1	Vertical distance between the drag force vector and the point around which rolling occurs
l_2	Horizontal distance between the lift and adhesion force vectors
L	Contact length between the droplet and solid surface
m	Weight of droplet
$m^{'}$	Correlated weight of droplet

M_D	Moment of surface stress
n	Stirring rate
N	Number of data points
O	Oil phase
r	Needle radius
$r^{'}$ and $r^{''}$	Principal radii of curvature
r_c	Radius of contact area
R	Radius of the particle/droplet
R_s	Radius of sphere
Re	Reynolds number
S	Solid surface
u	Velocity of fluid
v	Velocity of droplet/particle
V	Volume of droplet
V_{cap}	Volume of spherical cap
W_{AB}	Adhesion energy between A and B in vacuum
W_{ABC}	Adhesion energy between A and B in C
W	Brine/Water
wt%	Weight Percent
x	Measured value
$\overline{x}$	Average value
Å	Ångstrøm

Contents

Chapter 1

Introduction

Hydrate plugging is a substantial problem in the oil and gas industry, both economically, environmentally and safety wise. Plugging may occur as a result of agglomeration of hydrate particles, deposition of hydrates on the pipeline wall, large hydrate particle loadings or a combination of the three. It would be an advantage to have the hydrates following the flow as a dispersion, instead of agglomerating and depositing onto the pipeline wall. This would prevent plugging. To do this, knowledge about the force between the hydrate and the pipeline material is required.

The goal of this work is to enhance the understanding of hydrate deposition onto a pipeline wall and the forces between hydrates and pipeline materials. This is investigated through the contact angles and adhesion forces between water with hydrate former and different pipeline materials. A experimental setup has been developed which makes it possible to investigate the flow rate required to detach either a water droplet containing hydrate former or hydrates from various pipeline wall materials. Measuring of dynamic contact angles is used to estimate the force needed to detach a deposited brine droplet with a flowing fluid.

Chapter 2

Hydrates

A clathrate gas hydrate is natural gas and water crystallized to a solid, ice-like compound. The gas molecules (guests) are trapped in water cavities (host) that are composed of the hydrogen-bonded water molecules.

The word "'clathratus"' is Latin and means "to encage". The name refers to how the water molecules "encages" the gas molecule. Only eight natural gas components and an infinite number of natural gas mixtures form hydrates. Typical natural gas molecules include methane, ethane, propane, and carbon dioxide [1].

A hydrate can also be a salt with associated water, which is commonly used in laboratory experiments.

2.1 The history of natural gas hydrates

The scientific history of hydrates began around 1810, when hydrates was seen as a scientific curiosity. In 1934 the investigation of hydrates as a hinder in the production of oil and gas started after Hammerschmidt discovered the first hydrate plug in a petroleum pipeline [2]. In the mid-1960s the discovery of natural hydrates in both deep oceans and permafrost regions, as well as in extraterrestrial environments began. These reservoirs are now subject to research as they might be a future energy source or a climate hazard [3, 4, 5].

2.2 Formation of hydrates and the equilibrium curve

Gas molecules can form hydrates when three factors are fulfilled: available water, low temperature and high pressure. This means typically temperatures below 27° C and pressure above 6 bar, which is common in pipelines in cold environments and in deep ocean drilling. A sketch of a hydrate equilibrium curve can be found in figure 2.1.

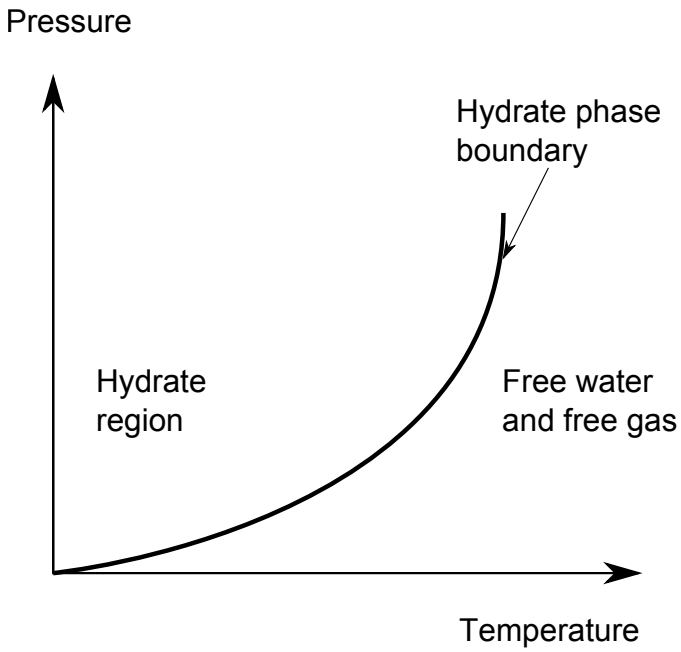

Figure 2.1: Illustration of a hydrate phase diagram. Hydrates are formed at low temperature and high pressure.

2.3 Hydrate structures

Clathrate hydrates are built by repetitive crystal units, composed of asymmetric, spherical-like "cages" of water molecules. Water molecules forms hexagonal rings that are held together by hydrogen bonds to form cages with different structures. Unlike ice, which is composed solely by water, hydrates have a guest molecules inside the cage. The guest molecules are held within the cage by dispersion forces, making the structure stable. This stability allows hydrates to form at temperatures above the formation temperature of ice, 0°C. Still, more than 85% of the hydrate consists of water, so the properties of hydrates resemble those of ice [1].

Which structure the hydrate forms depends on the type and size of the guest molecule. The most common hydrate structures are I (cubical), II(cubical) and H(hexagonal) [1], as illustrated in figure 2.2. Structure I is formed when the guest molecules are small, with diameter less than 6Å, such as methane, ethane, carbon dioxide and hydrogen sulfide. Larger, but still small molecules such as nitrogen form structure II. These guest molecules have diameter between 6 - 7Å. Even larger molecules with diameter up to 9Å, like iso-pentane or neohexane, can form structure H when accompanied by smaller molecules such as methane, hydrogen sulfide or nitrogen. Structure H is more unusual than structure I and II [7]. Note that hydrates are non-stoichiometric, since the number of guest molecules varies [7].

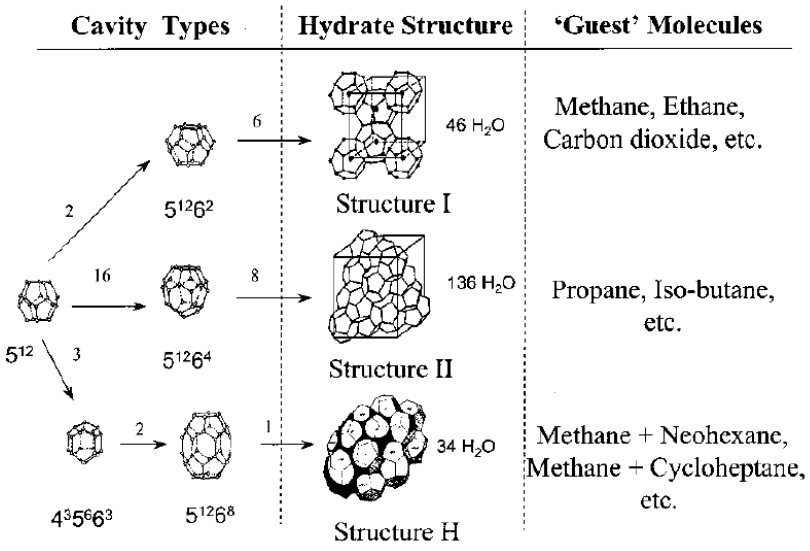

Figure 2.2: Three common hydrate unit crystal structures. Nomenclature: $5^{12}6^4$ indicates a water cage composed of 12 pentagonal and 4 hexagonal cages. The numbers along the lines indicates the numbers of cage types. Example: the structure I crystal is composed of 2 5^{12} cages, 6 $5^{12}6^2$ cages, and 46 water molecules. Figure is from Sloan [6].

2.4 Formation of hydrates in pipelines

Little is known about the actual hydrate growth process, but hydrate crystals may grow either in the aqueous phase, on a particle in the aqueous phase ("seed"), on the pipe wall, or on gas - liquid interfaces if water is present in sufficient amounts. The deposition will mainly be influenced by the following factors [8]:

- Degree of sub cooling
- Wall heat flux
- Internal cooling
- Flow rate
- Fluid properties and emulsification of the liquid phases
- Condensation profile

Initial growth typically takes place at the pipe wall above the liquid - gas interface when water condenses at the pipe wall. The pipe wall has the lowest temperature due to heat transfer with the outside environment, and will therefore be the first point to have the right temperature.

It has been found that as the hydrate layer grows, the temperature increases as a result of the solid deposition acting as insulation, reducing the wall heat flux. This will slow down the rate of hydrate growth [8, 9].

2.4.1 Oil-dominated systems

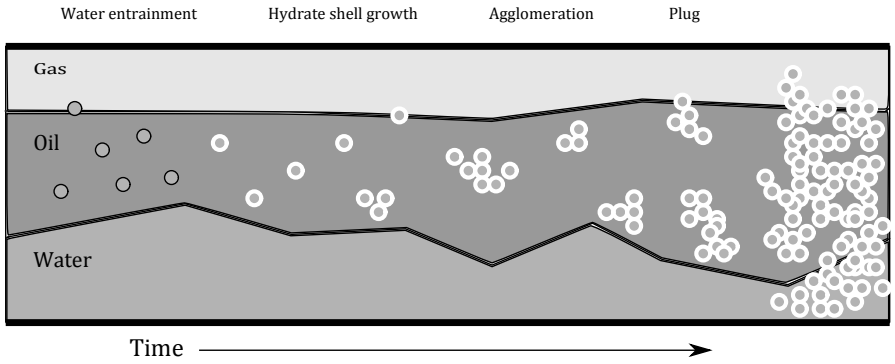

Figure 2.3: The figure shows the formation of a plug in an oil-dominated system, illustrating the system initially consists as a water-in-oil emulsion, before hydrate shells forms around the water droplets and capillary forces cause the shells to agglomerate into plugs. This figure is redrawn from Sloan [1].

Sloan [1] operates with six steps in the formation of hydrate plugs in an oil-dominated system.

1. The water phase is emulsified within the oil phase.

2. A thin (perhaps smaller than six microns thick) hydrate shell grows around the water droplets.

3. The hydrate shells form a diffusional barrier between the hydrocarbon and water phases.

4. Capillary forces of attraction cause the hydrate-encrusted droplets to agglomerate.

5. As the particles agglomerate, the effective viscosity increases dramatically, until finally the clusters become sufficiently large to increase the pressure drop leading to shut-in flow.

6. As the plug sits for a longer period of time, the masses anneal and the plug becomes more solid-like, with less flexibility. That is, both intra- and inter particle growth occurs (not shown in the figure).

This is illustrated in figure 2.3.

2.4.2 Gas-dominated systems

In gas-dominated systems, compared to oil-dominated, there is much less liquid.

Sloan [1] suggests five steps for hydrate formation in a gas-dominated system:

1. There is water in the pipeline due to produced water and condensed water from the gas.
2. Condensed vapor and/or splashing deposits water on the pipe wall. As previously mentioned, the pipe wall has the lowest temperature, and consequently is the point of the first hydrate deposition.
3. As the hydrate layer on the wall becomes thicker, the pressure drop increases.
4. When the hydrate layer is thick enough, the weight of the layer and the stress from the passing fluid becomes too much, and hydrate agglomerates dislodge from the wall. This can be noticed as a decrease in upstream pressure.
5. Dislodged particle agglomerates may travel downstream and bridge across the flow channel to form a plug.

2.5 Hydrate inhibitors

Much research has been put into the avoidance of hydrate plugs. The most obvious way is to avoid the hydrates from forming. To form hydrates, water and suitable guest molecules are needed, along with proper temperature and pressure. If one of these factors is absent, hydrates will not be formed. This way of avoiding hydrates is called physical inhibitors, but can be difficult to use in practice. A reservoir naturally contain water, which will follow the stream of oil/gas. This water is difficult and expensive to remove. Pressure is needed to move the flow, so depressurizing is mostly not an option. The oil/gas is warm from the reservoir, but is cooled by the cold environment often surrounding the pipelines. Insulation will maintain the high temperature up for a longer time, but only for a limited length. Electrical heating is also a possibility, however an expensive one.

The most common way to avoid hydrates from forming is to use thermodynamic inhibitors [1]. They bond to the free water and reduce the activity so that even lower temperature and higher pressure is required to achieve hydrate formation. Hence the equilibrium curve is shifted. Most commonly used thermodynamic inhibitors are methanol (MeOH) or monoethylene glycol (MEG). The problem with thermodynamic inhibitors is that they require high dosage, often 15-50wt% of the water content of the flow [10]. Regeneration is an expensive process and the chemicals are toxic, making thermodynamic inhibitors both expensive and not environmentally friendly.

A less expensive alternative is low-dosage hydrate inhibitors (LDHI). They are called low dosage because the concentration can be as low as 0,3-0,5wt%. With such a low dosage, they do not change the bulk phase properties, only the interfacial properties.

LDHI can be divided into two types that act very differently. Kinetic inhibitors (KI) adsorb on the hydrate - water interface and slow down the rate of growth, while anti agglomerants (AA) keep the particles from agglomerating or depositing. AAs are part of a new trend moving from total avoidance to risk management. Hydrates are allowed to form, but hydrophobic, surface-active molecules adsorb on the hydrate surface, and probably also the pipeline wall. These keeps the hydrates from agglomerating, so that a transportable hydrate slurry is formed instead of hydrate clusters [10, 11].

2.6 Natural inhibiting components

It has been found that the tendency to form hydrate plugs varies for different crude oils [8, 12, 13]. Even within the thermodynamic stability zone, some crude oils do not form plugs. Several authors have indicated that the plugging tendency of crude oil is dependent on the presence or absence of natural inhibiting components (NICs) [14, 15]. Possibly, surface active compounds, act as anti agglomerants, preventing the small hydrate particles from forming large plugs. These NICs are found to be extractable from crude oils [14].

Chapter 3

Equipment

This chapter gives a description of the different tools used in the experiments and calculations. This involves surfaces, chemicals, camera, computer software, statistical equations.

3.1 Hydrate models

In this project, the experimental work does not involve natural gas hydrates, since they require very high pressure and low temperatures, and therefore are difficult and dangerous to work with. Instead, models for natural gas hydrates, denoted as hydrate formers, are used. Those are both easier and safer to work with. The type of hydrate former was chosen based on miscibility with petroleum ether, hydrate structure, hydrate formation temperature, toxicity and volatility.

3.1.1 TBAB hydrates

TBAB (tetra-*n*-butylammonium bromide $(C_4H_9)_4N\,Br$) is a salt that forms semi-clathrate hydrates at atmospheric pressure and near room temperature [1]. TBAB forms hydrates of either structure I or II, depending on the concentration and temperature. A picture of a TBAB hydrate structure can be found in figure 3.1. The phase diagram of TBAB can be found in figure 3.3. An aqueous solution of $\geq$40 wt% TBAB only form structure II hydrates, and formation can occur up to 12° C at 1 atm. An aqueous solution of $\leq$20 wt% TBAB may form either structure I or structure II hydrates, depending on the temperature [18]. 15 wt% TBAB is used in the experiments, which gives structure I hydrates for the temperatures in question. Being a salt, it is only soluble in the water phase. More information about TBAB can be found in table 3.1.

3.2 Solid surfaces

The solid surfaces investigated are stainless steel (AISI 316 L), aluminum (EN AW 5052), brass (63% Cu, 37%Zn), glass and an epoxy coating, as shown in figure 3.4. More

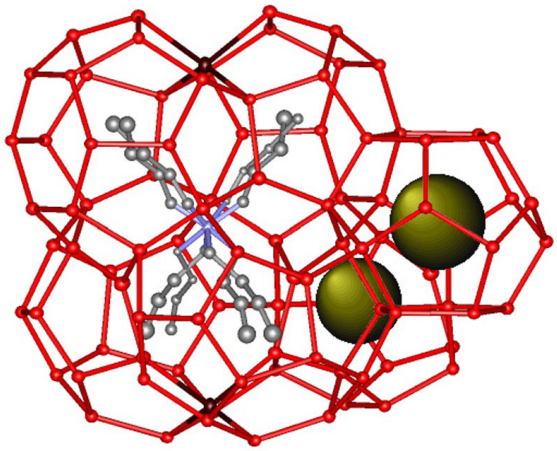

Figure 3.1: The figure shows a TBAB hydrate structure. Picture from Shimada et al. [16].

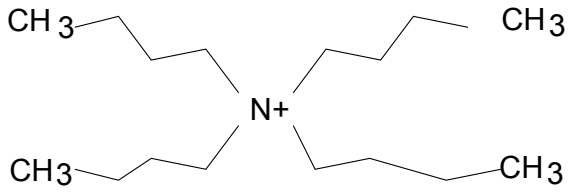

Figure 3.2: The figure shows a TBAB structure [17].

Manufacturer	Sigma-Aldrich
Linear formula	$(CH_3CH_2CH_2CH_2)_4N(Br)$
Molecular Weight	332,37g/mol
Assay	$\geq$99.0% (AT)
Hazard	Irritant

Table 3.1: Tetrabutylammonium bromide properties [17].

information about the surfaces and epoxy coating can be found in the work of Aspenes [13].

3.3 Chemicals

3.3.1 Petroleum ether

Petroleum ether was used as a model oil in all experiments. More information about petroleum ether can be found in table 3.2 and the results from an infrared spectroscopy can be found in the appendix, in section D.

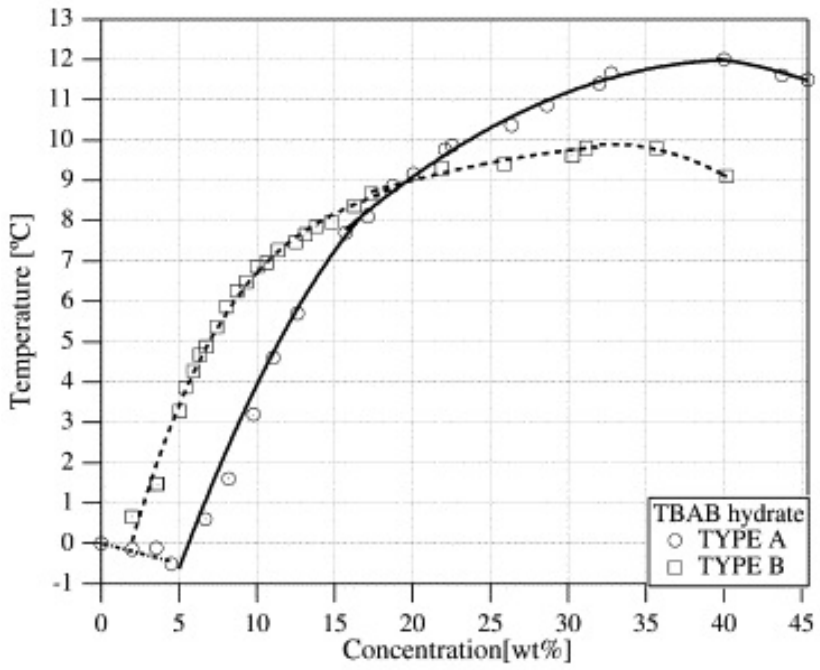

Figure 3.3: The figure shows the typical equilibrium curve for the two different structures of TBAB. The diagram is the work of Oyama [18].

Synonym	Petroleum benzin
Grade	Puriss. p.a.
Boiling Point	60-80°C
Density	0.660-0.680 g/mL at 20°C
Viscosity	0.0003 kg/ms
Hazard	Highly Flammable
	Harmful
	Dangerous for the environment

Table 3.2: Petroleum ether properties [19].

3.4 Equipment used to study the hydrates and droplets

A microscope, a camera and a stirrer were used to study the hydrates and droplets. A picture of how they were put together can be seen in figure 3.5.

3.4.1 Microscope

A microscope was needed to investigate the contact angles and how the hydrates grew. The microscope, model SMZ800 from Nikon, was borrowed from SINTEF. More infor-

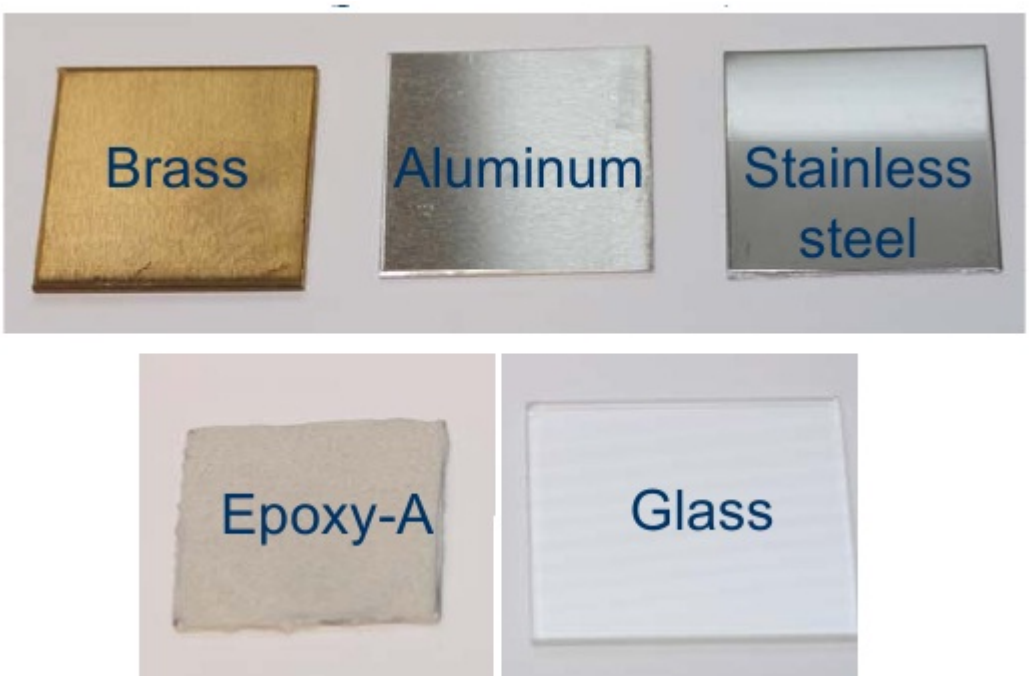

Figure 3.4: The surfaces used in the experiments. The surfaces are brass, aluminum, stainless steel, epoxy-coated surfaces and optical glass. The size of each plate is approximately 3x3 cm. The picture is from the PhD thesis of Aspenes [12].

mation about the microscope can be found in table 3.3.

Supplier	Nikon
Total magnification	5X - 378X
Zoom range	1X - 6.3X
Zoom ratio	6.3 : 1

Table 3.3: Specifications of the SMZ800 Microscope from Nikon [20].

3.4.2 Camera

The camera was used for many purposes. To find contact angles, pictures were taken of each droplet and used for digital investigation. To find the dynamic contact angle of the droplet in a flowing fluid, the camera was set to make a live video, then the right picture could be taken out. It was also useful and interesting to have a camera to see how the hydrates formed and grew.

The camera used was a Retiga EXi digital camera, borrowed from SINTEF. This camera is very sensitive to light, making it possible to take pictures even in the sparse light in the refrigerator. The camera has a progressive scan interline CCD sensor which

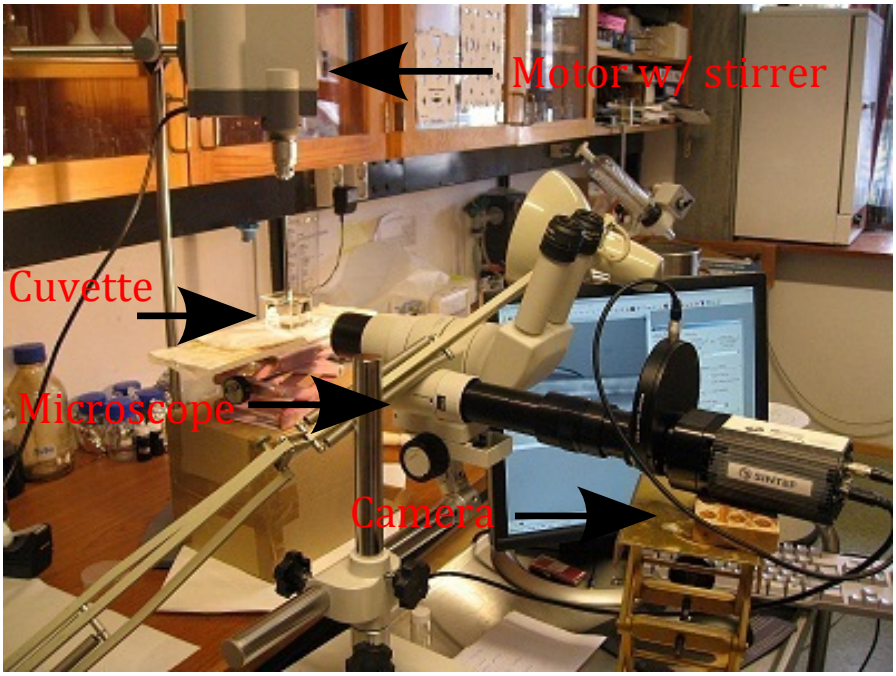

Figure 3.5: The picture shows how the microscope, the camera and the cubical container was set up to take pictures of the droplets. The motor can be seen above the cuvette.

gives 1.4 million pixels in a 12-bit digital output, making it suitable to investigate details. The IEEE1394 FireWire output of the camera made it easy to install and use. A High-Speed Readout makes it possible to take see preview in real time and to make live video. More information about the camera can be found in table 3.4.

The camera was connected to the microscope.

Supplier	QImaging
Maximum resolution	1392 x 1040
Frames per second	10 - 165
Capture time	10 s - 17.9 min
Operating temperature	0 - 50°C
Digital output	12-bit
Output	FireWire IEEE1394

Table 3.4: Specifications of the QImaging Retiga EXi digital camera [21].

3.4.3 Motor

The stirrer used in the particle detach experiments is a VOS Power Control delivered by VWR. It has analog display that makes it easy to read the speed. A smooth start makes it safe to use, which is important when the observer has to be close to the setup. It is

build for mixing large particles or mixtures of medium viscosity. Picture of the motor can be found in figure 3.6 and specifications can be found in table 3.5.

Supplier	VWR
Maximal stirring capacity (liters of water)	40
Maximal viscosity (cps)	50 000
Speed Range (rpm)	50-2000

Table 3.5: Specifications of the VWR VOS Power Control [22].

Figure 3.6: The motor VOS Power Control from VWR [22].

3.4.4 Stirrer

The stirrer used is a three bladed propeller stirrer from IKA, model R1311. The stirrer generates axial flow which makes it ideal for these kind of experiments. It has a diameter of 30 mm and maximum speed of 2000 rpm. Picture of the stirrer can be found in figure 3.7.

Figure 3.7: The stirrer, model R1311 from IKA [23].

3.5 Software

3.5.1 STAR CD

Computational Fluid Dynamics (CFD) is one of the three approaches to fluid dynamics, the other two being theory and experiments. CFD uses computers and algorithms to numerically solve physical problems. CFD results are directly analogous to experimental results obtained in a laboratory and a CFD program is said to be a "transportable wind tunnel" [24].

STAR CD is a CFD software delivered by CD-adapco and is a an integrated platform developed to tackle problems involving multi-physics and complex geometries.

3.5.2 Image-Pro Plus

Image-Pro Plus is an image, enhancement and analysis software delivered by MediaCybernetics.

3.6 Statistical equations

The uncertainty is an important part of information about any experimental result, without it, the result may be useless.

Standard deviation is the most used measure for uncertainty and measures how much a series of measured values deviates from the average value of the data points [25]. A low standard deviation indicates that the data points tend to be very close to the mean, and vice versa. The formula for standard deviation is:

$$\sigma = \sqrt{\frac{\sum (x - \overline{x})^2}{N}} \tag{3.1}$$

where σ is the standard deviation, x is the measured value, $\overline{x}$ is the average of all measured data points and N is the number of data points. The average, $\overline{x}$ is given by:

$$\overline{x} = \frac{1}{N} \sum x \tag{3.2}$$

Chapter 4

Solid surface wetting properties

Pipeline surface properties may influence deposition of hydrates to the pipeline wall. Important surface properties are wettability and adhesion energy, which can be quantified through the contact angle.

4.1 Background and literature survey

Hydrates in a petroleum pipeline are expected to grow and form plugs as described in section 2.4. In gas-dominated systems, a liquid water droplet deposits on the wall and the hydrate grows from this droplet [1]. The energy acting between the droplet and the pipeline wall can be quantified through the adhesion energy and the wettability.

Some research has been done to investigate the forces between hydrates and different pipeline materials and the effect of flow. Aspenes et al. [12] investigated contact angles and adhesion energy between water and different surfaces in the presence of oil, and the surface free energy of different surfaces. The effect of presence of acid was also investigated, and it was found that both the presence of petroleum acids in the oil (and low surface free energy of the pipeline material) lead to more oil-wet systems and reduced adhesion energy. dos Santos et al. [26] investigated the contact angles of oil droplets of crude oil on glass, commercial and galvanized steel surfaces immersed in 1 wt% sodium chloride solution. It was found that glass had much lower contact angle (more water-wet) than the metals.

4.2 Theoretical background

When evaluating pipeline surface materials with regards to hydrate deposition, the most important properties are suggested to be: Wettability, surface free energy, roughness and surface charge [13]. Wettability is evaluated in this work.

4.2.1 Surface properties

The chemical and physical properties of substances are dependent on the forces acting between molecules.

The molecular forces acting inside a medium gives rise to the surface tension or surface energy, γ. A molecule in a bulk of the same molecules is pulled from all sides by the same force, and the net force moving the molecule in any direction. A molecule near a surface, however, have less neighboring molecules and is therefore pulled more by the molecules in its own bulk, as illustrated in figure 4.1, and experiences a net force acting inwards, away from the surface. Thus, a force is needed to transport a molecule to the surface. This means the work most be done to increase a surface area.

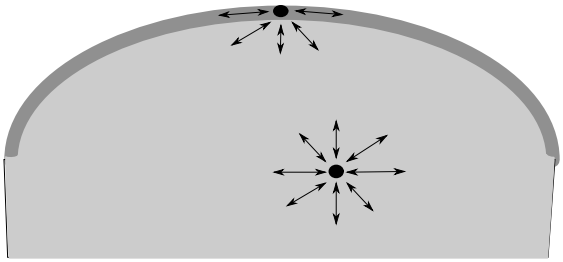

Figure 4.1: Surface tension: This illustration shows how the molecules at the surface experiences a net force towards the bulk, creating the surface tension.

Surface tension is defined as the force needed to extend the surface area by one unit, and has the unit Nm^{-2} [27].

A smaller surface area means less molecules at the surface and is therefore energetically favorable, explaining why droplets tend to be spherical [28].

For solids, γ is commonly denoted by γ_S and is given in units of energy per unit area: mJ m^{-2}. For liquids, *interfacial energy* or *interfacial tension* is often used instead of surface tension, with γ_1 commonly denoted by γ_L and usually given in units of tension per unit length: mN m^{-1} [27]. In this work, S denotes the solid surface, O denotes the oil phase and W denotes the water or brine droplet.

In the meeting between different substances or different phases, there are forces acting between the different molecules, determining the shape and behavior of the system. These forces can be quantified through the *adhesion energy*.

The adhesion energy is defined as the energy required to separate unit areas of two different media from contact to infinity, often written W_{12} [27]. This is illustrated in 4.2.

The adhesion energy in vacuum is always positive since all media attract each other in vacuum. But in a third medium it can be both positive and negative, depending on the type of interaction [27].

The connection between surface tension and adhesion energy is that the process of creating one unit area of surface is equivalent to separating two half-unit areas of the

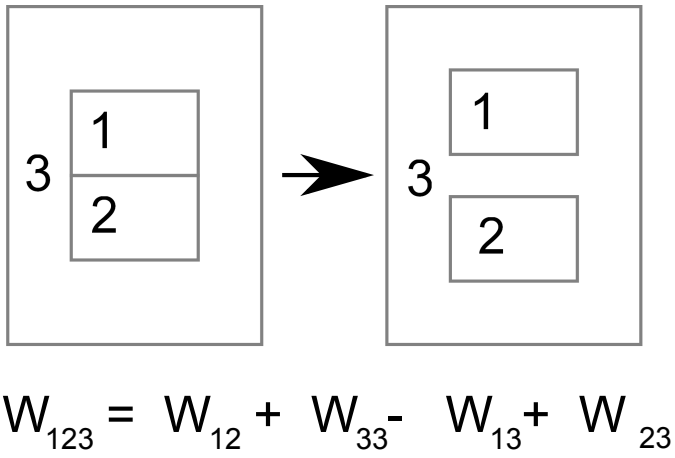

Figure 4.2: Illustration of work of adhesion in a third medium. This figure is redrawn from Israelachvili [27].

same medium from contact, giving

$$\gamma_1 = \frac{1}{2} W_{11} \tag{4.1}$$

4.2.2 The Young Dupré equation

As mentioned, the energy between the molecules determine the shape and properties of a system. For a system consisting of a brine droplet on a rigid, solid surface in oil, the shape of the droplet to the surface is determined by the interfacial tension between the droplet and oil, between the droplet and the surface and between the surface and oil, as illustrated in figure 4.3.

In the figure, γ_{SO} is the interfacial tension between the solid and oil phase, γ_{SW} is the interfacial tension between the solid and water phase and γ_{WO} is the interfacial tension between the water phase and the oil phase θ is the contact angle

When the system is in equilibrium, the sum of the vectors is zero, and the force balance resolved in horizontal direction can be written as:

$$\gamma_{SO} = \gamma_{SW} + \gamma_{WO} \cos\theta \tag{4.2}$$

called Young's equation [29, 30]

This angle θ is called the contact angle and quantifies the wettability of the system. If the forces between the droplet and the surface are larger than those between the droplet and the surrounding fluid, the droplet will spread on the surface and the contact angle will be low. And vice versa. How much the droplet spreads on the surface is called wettability and is quantified through the contact angle. The contact angle is defined to be measured through the aqueous phase.

If θ approaches 0°, the liquid and the surfaces has a large contact area, the interaction between the liquid and the surface is strong and the system is said to be perfectly wetting.

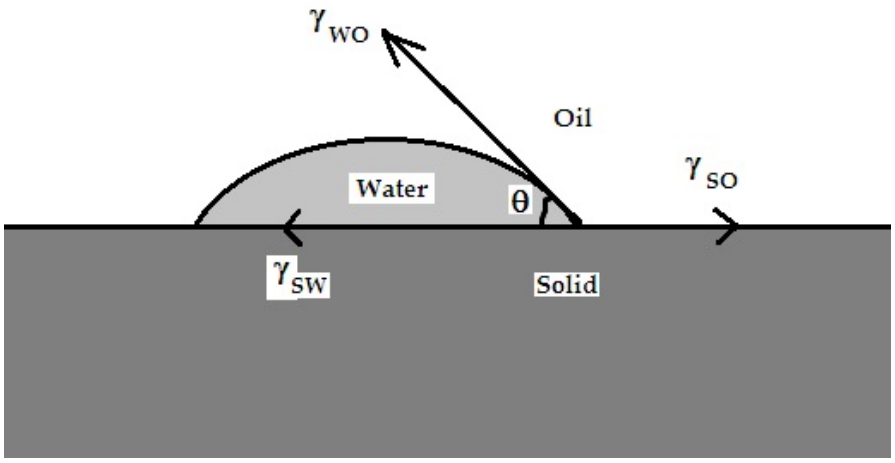

Figure 4.3: Brine droplet deposited on a surface surrounded by an oil phase, with belonging force vectors.

Opposite, if the angle approaches 180° it is perfectly unwetting and the liquid interacts weakly with the surface. In the latter case, the droplet will be more or less circular. In general, if the angle is less than 90° the liquid is considered to wet the surface, whereas angles higher than 90° correspond to nonwetting [30].

Young's equation can be rewritten into the Young-Dupré equation [27]:

$$W_{SWO} = \gamma_{WO}(1 + cos\theta) \tag{4.3}$$

This equation gives the adhesion energy, W_{SWO}, per unit area of a solid surface from a combination of the interfacial tension γ_{WO} of the brine in oil and the contact angle θ.

4.2.3 Contact angle hysteresis

The contact angle is a thermodynamic quantity, and should therefore be expected to be a unique value for any particular system. But for real surfaces, this is often not the case. The reason why is an on-going debate, but there are mainly two effects that are suggested:

- physical heterogeneity, such as surface roughness
- chemical heterogeneity, either in the solid surface, or by slow adsorption and desorption of solute molecules dissolved in the liquid.

Experiments have been performed to find out if very long equilibration times give unique contact angles, but none of these experiments have succeeded. [27, 26].

4.2.4 Measuring surface tensions of liquids; the droplet-weight method

To measure the surface/interfacial tension between a liquid and air or a liquid and another liquid, the droplet-weight or droplet-volume method is commonly used. The method was developed by Harkins and Brown in 1919 [31]. The equipment used in this method can be seen in figure 4.6, in section 4.3.2.

To measure the surface tension between a liquid and air, a syringe needle is filled with the liquid in question and a droplet is carefully pressed out of the tip. The force between the droplet and the needle is equal to the surface tension times the circumference of the needle and keeps the droplet from falling off. When the droplet becomes too big, the weight of it will exceed the force exerted by the surface tension between the droplet and the needle, and the droplet will fall off. The force balance is then:

$$2\gamma\pi r = mg \tag{4.4}$$

In this equation, m is the weight of the droplet, g is the acceleration due to gravity, r is the radius of the needle and γ is the surface tension.

In practice, not all of the droplet will fall from the needle, and a correction factor, F, has been developed to compensate for this. The measured mass, m', is smaller than the mass in the real force balance, m, so the modified force balance becomes:

$$2\gamma\pi rF = m'g \tag{4.5}$$

To measure the liquid-liquid interfacial tension, as is done in this work, the method is similar, but the needle is filled with one liquid and immersed in the other. A droplet is pressed out, but the volume, V, instead of the weight is measured. The buoyancy is taken into account by the density difference $\Delta\rho$, and the rewritten force balance becomes:

$$\gamma = \frac{V\Delta\rho g}{2\pi rF} \tag{4.6}$$

This method is called the droplet-volume method, since the volume is measured rather than the weight. In this case the correction factor is expressed by:

$$F = 0.4293(\frac{r}{V^{1/3}})^2 - 0.7249\frac{r}{V^{1/3}} + 0.9054 \tag{4.7}$$

.

4.3 Experimental

The experiments were performed at ambient temperature, approximately 21°C. The surface was placed at the bottom of a cubical cuvette and the cuvette was filled with a model oil, petroleum ether, described in section 3.3.1.

Prior to use, the surfaces and the cuvette were washed in sodosil, rinsed with tap water, distilled water and ethanol, and dried with nitrogen gas.

A droplet of 15 wt% TBAB (see section 3.1.1) was deposited onto the surface, using a syringe. It was left to settle for approximately 5 minutes before a picture was taken, using a microscope (SMZ800) from Nikon connected to Retiga Exi fest 1394 digital camera from QImaging. The camera and microscope are described in section 3.4. This setup was connected to a computer with the software ImagePro Plus installed. A sketch of the setup can be seen in figure 4.4.

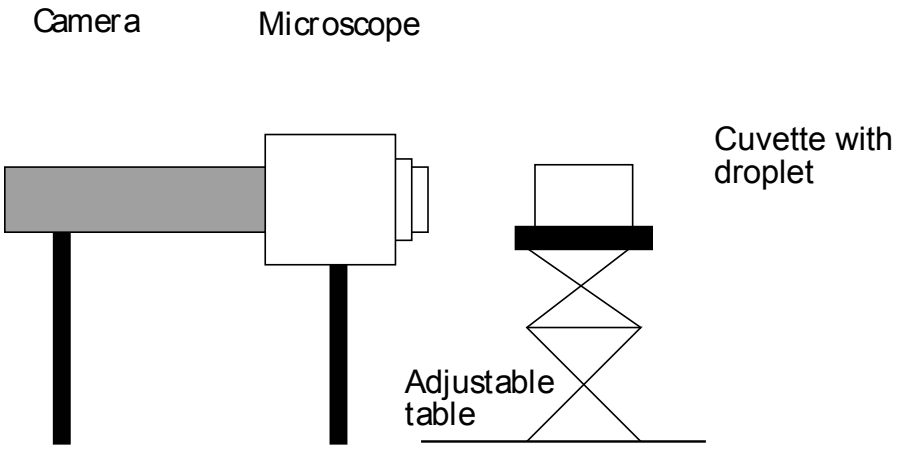

Figure 4.4: The picture shows how the microscope, the camera and the cubical container was set up to take pictures of the droplets.

4.3.1 Contact angle

Contact angles were measured from images of droplets using a software package, Image-Pro Plus. ImagePro Plus has a function which allows the user to manually set the angle as shown in figure 4.5. This was done five times on each side and the average of these was used. This method is subject to some degree of subjectivity [12]. For each surface, five to ten different droplets were measured.

Another powerful method to evaluate the contact angles is to use an axisymmetric drop shape analysis-profile (ADSA-P) method. This method uses the complete drop shape profile and a combination of interfacial tension, the difference in density between the two phases and gravity to determine the contact angles [32], and the degree of subjectivity is therefore smaller than the method described above. A MatLab-routine using ADSA-P, developed by Kjell Askvik was used on some of the images, but for reasons unknown, this did not work for most pictures, so the results are not used.

4.3.2 Interfacial tension

Interfacial tension between water with 15 wt% TBAB and petroleum ether, γ_{WO}, was measured using the drop weight method described in section 4.2.4. A picture of the setup can be found in figure 4.6. The volume of the brine in the syringe was recorded,

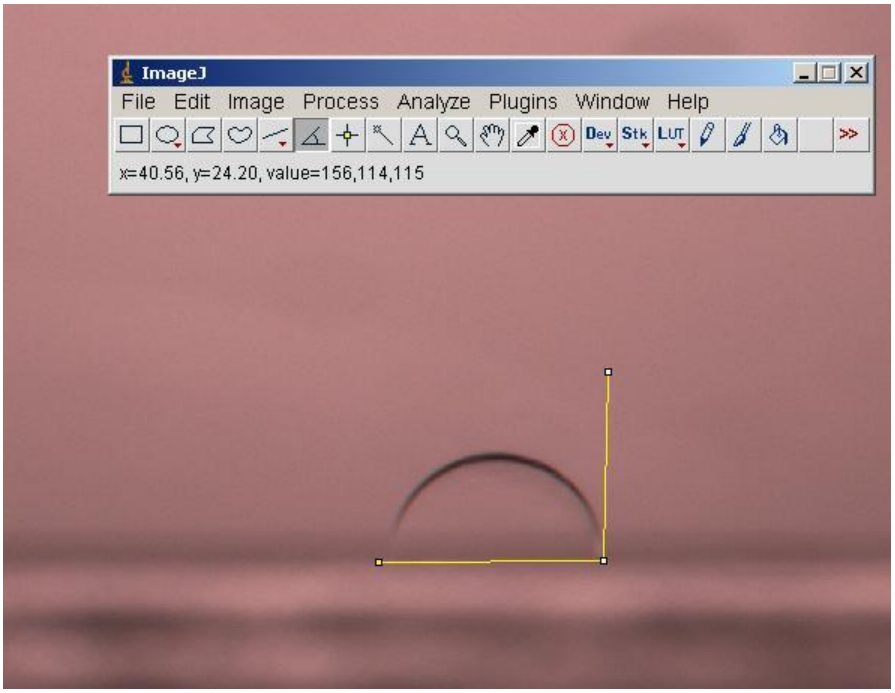

Figure 4.5: The angles were found with ImagePro, setting the angle five times at each side.

and ten droplets were carefully pressed out of the syringe by twisting the upper part, and the volume was recorded again. The difference in the volume before and after was used to find the volume of one droplet. This droplet was used as input in formula 4.6 to find the interfacial tension.

Densities of both phases were found by measuring the weight of a known volume.

4.4 Results

4.4.1 Contact angle and adhesion energy

The contact angle between a liquid droplet of water with 15 wt% TBAB deposited on different solid surfaces in petroleum ether was measured at ambient temperature. Examples of images of droplets can be seen in figure 4.7. The contact angles were combined with the interfacial tension between the brine and petroleum ether using the Young Dupré equation (4.3) to calculate the adhesion energy. The results are shown in table 4.1 and figure 4.8 and 4.9. The whole data set and images of the droplets can be found in the appendix, in section A.1 and A.2. There were some diffenence between the left and right contact angles on the droplet; the contact angle is the average of the two.

γ_{WO} was found to be 10,71mN/m.

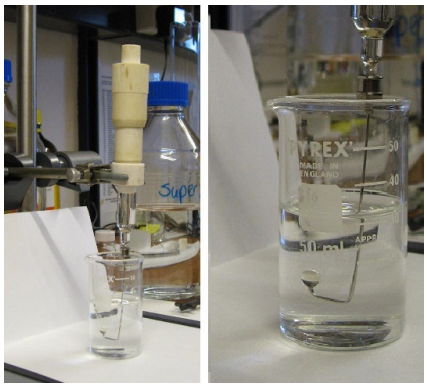

Figure 4.6: The figure shows the equipment used in the droplet-weight method. A droplet can be seen on the tip of the syringe.

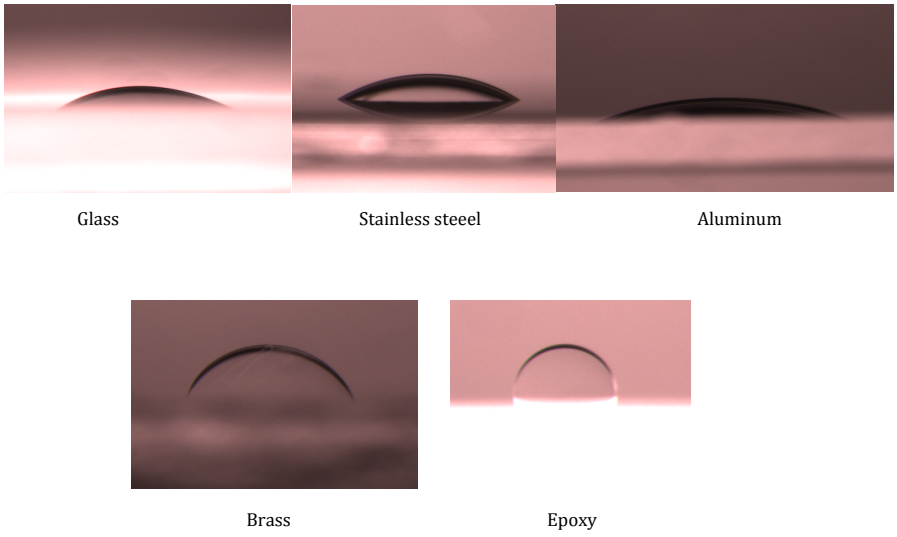

Figure 4.7: Pictures of brine droplets on different surfaces. The other edge of the droplet on the stainless steel surface, is the droplets reflection.

4.5 Discussion

Table 4.1 and figure 4.8 shows the contact angles between water with 15 wt% TBAB and different surfaces in the presence of petroleum ether.

It was found that the contact angles and thus adhesion energy do vary for the different surfaces in question. The glass, stainless steel and aluminum surfaces all have low contact angles, and the brine can be said to wet the surface. The epoxy surface stands out with a significantly higher contact angle as seen in table 4.1. With a contact angle higher than 90°, epoxy is the only surface in this experiment that can be said to be oil-wet. This indicates that the adhesion energy between brine and epoxy surface in the presence

Surface	Contact angle (degrees)	Adhesion energy W_{SOW} [mN/m]
Glass	32 ± 5	20
Steel	29 ± 6	20
Aluminum	25 ± 5	20
Brass	63 ± 20	16
Epoxy	97 ± 4	9

Table 4.1: The adhesion energy between water with 15 wt% TBAB and different surfaces in the presence of petroleum ether.

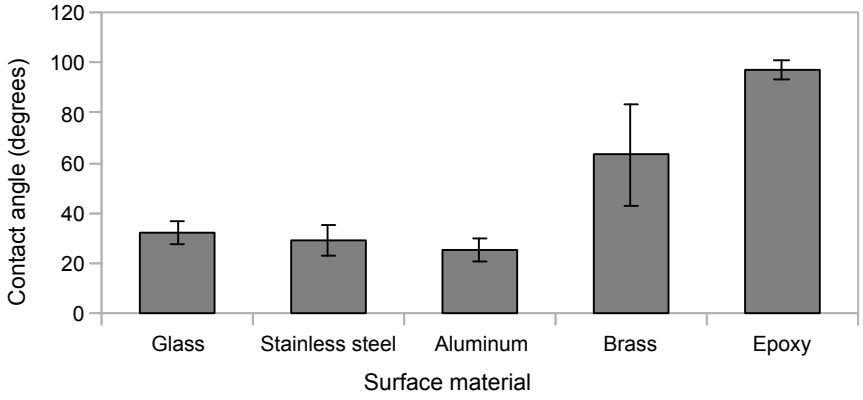

Figure 4.8: Contact angle between 15 wt% TBAB and different surfaces in the presence of petroleum ether.

of petroleum ether is lower than for the other surfaces and the aqueous phase has less tendency to stick to epoxy, compared to the other surfaces.

One possible mechanism for hydrate growth is that the hydrates start to grow from droplets on the pipeline wall. A pipeline made of a material that is oil-wet rather than water-wet, means that water droplets are less likely to stay on the wall. It can also be expected that a hydrate formed in a steam, will be more likely to deposit onto and stay on a water-wet wall, than an oil-wet wall. If that is the case, an oil-wet pipeline wall, such as epoxy, has a lower possibility of hydrate growth and plugging.

The contact angles of glass, stainless steel and aluminum are all within an interval of 7°, indicating that the wettability and hence the probability for hydrate deposition and growth on these surfaces is approximately the same.

The uncertainties of these experiments are quite high, between 4° and 6° for glass, stainless steel, aluminum and epoxy, and 20° for brass. Figure 4.10 shows images of droplets sitting on a brass surface, and table 4.2 gives measured contact angles. It can be seen that there is a large spread in the contact angles. The lowest angle, 31° indicates that brass is a water-wet surface, while the highest angles, 104° indicates the opposite. The average contact angles indicates that brass is slightly water-wet.

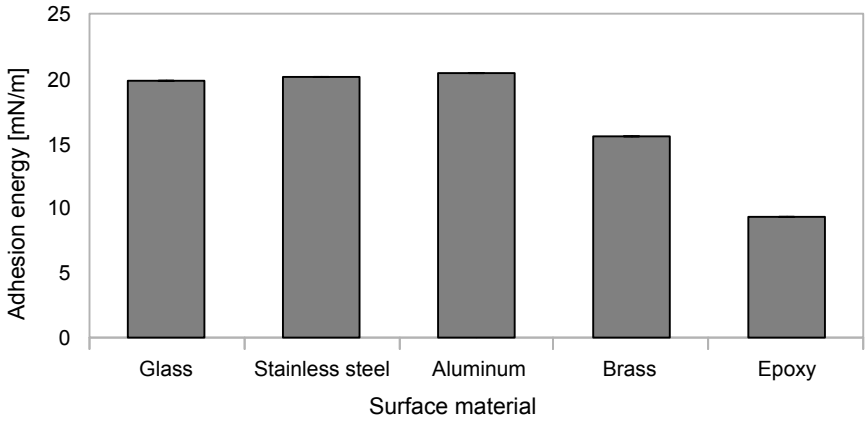

Figure 4.9: Adhesion energy between 15 wt% TBAB and different surfaces in the presence of petroleum ether.

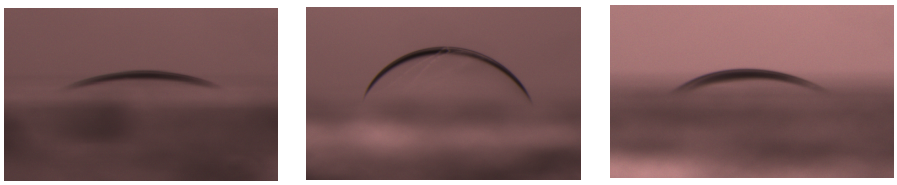

Figure 4.10: Droplets of brine sitting on a brass surface. Brass was the surface that had contact angles with the largest standard deviation.

Surface	Left angle (degrees)	Right angle (degrees)
Droplet 1	89 ± 3	88 ± 2
Droplet 2	70 ± 5	90.3 ± 0.9
Droplet 3	75 ± 6	72 ± 8
Droplet 4	33 ± 3	36 ± 2
Droplet 5	31 ± 3	26 ± 2
Droplet 6	69 ± 2	75 ± 3
Droplet 7	73 ± 2	72 ± 2
Droplet 8	58 ± 3	55 ± 2
Droplet 9	104 ± 2	111 ± 1

Table 4.2: Measured droplets on brine sitting on a brass surface.

Not only did the shape of the droplets vary, there was also a difference between the left and right contact angle on each droplet, meaning that the droplets were not completely symmetrical. The largest difference was in a droplet on a brass surface, where the difference between the two contact angles was 20°. Most of the droplets had

a difference of 2-3°.

There can be many reasons for deviation in contact angles. One reason may be the degree of subjectivity when manually setting the angle in ImagePro Plus. Another may be that the surface was not totally plane, so that gravity would make the droplet not symmetrical. Contamination can locally alter the surface properties, as well as surface roughness. Some of these reasons were discussed in section 4.2.3.

A study of the roughnesses of the surfaces used in this work can be found in the PhD thesis of Aspenes [13]. Aspenes found results that indicate that the surface roughness influences the measured contact angles drastically. In this work, is was found that the epoxy surface has a significantly larger roughness than the other surfaces, but epoxy actually has the lowest standard deviation of the surfaces in this experiment, so surface roughness is probably not the only reason for the deviations.

4.6 Conclusion

It was found that the contact angles and adhesion energies are different for brine of 15 wt% TBAB and different surfaces surrounded by petroleum ether. Glass, stainless steel and aluminum all had low contact angles, 25-32°, and corresponding high adhesion energy. The brass surface was sligtly water-wet with a contact angle of 63°, and epoxy was the only oil-wet surface, with a contact angle of 97°. The indicates that water droplets will adhere more stongly to some surfaces, compared to others, depending on wetting properties.

Chapter 5

Effect of flow on the detachment of droplets and particles

The flow characteristic in a petroleum pipeline can be expected to be an important factor with regards to hydrate plugging. Not only does it affect the growth of hydrates in terms of mass transport and hydrates particle collisions, but also how or if hydrates grow or deposit on the pipeline wall.

The purpose of the experiments were to investigate the effect of flow on a hydrate particle on different surface materials. An experimental setup was developed which was easy to use with regards to depositing particles and changing surfaces.

Some of the gathered data was used in a used in a Computational Fluid Dynamics (CFD) simulation to estimate the drag force needed to dislodge a hydrate particle.

5.1 Background and literature survey

To remove particles from surfaces, one generally uses gravitational forces, centrifugal forces, mechanical forces or flowing forces. To measure force either between two particles or between a particle and a surface, micromechanical technique [9, 13, 33, 34], atomic force microscopy [35] or optical tweezers [36] are typically used.

Not much work has been done on investigating the forces between hydrate particles and surface materials. Groysman et al. [37] tried in Moscow in 1990 to use a scrape to detach tetrahydrofuran and freon hydrates from steel, an aluminum alloy and plastic. Aspenes et al. [38] used a micro mechanical setup and measured the force needed to detach cyclopenthae hydrates and different solid surfaces and two cyclopentane hydrates, with and without acid and free water in the system. The solid surfaces used in this work, are the same as those used by Aspenes.

The most common way to investigate the effect of flow on particle removal, is to use a flow loop [9, 39, 40, 41, 42]. This was tried by Aspenes et al. [43], but proved to be difficult.

5.2 Theoretical background

5.2.1 Quantification of flow: Reynolds number

A usual way to quantify flow is through the Reynolds number. It is dimensionless, and gives a measure of the ration of inertial forces to viscous forces. Which parameters goes into the Reynolds number varies for different problems and geometries. The dynamic viscosity of the fluid, μ, and the density of the fluid, ρ, are always included. The magnitude is independent of the units used.

In a pipe, Reynold number is $Re = \frac{D_{pipe} u \rho}{\mu}$, where D_{pipe} is the diameter of the pipeline and u is the average velocity of the fluid.

In a circular, stirred container, Reynolds number is $Re = \frac{D^2_{stirrer} n \rho}{\mu}$, where $D_{stirrer}$ is the diameter of the stirrer and n is the stirring rate.

The Reynolds number for a particle is defined to be $Re = \frac{du\rho}{\mu}$, where d is the diameter of the particle, and u is the velocity fluid.

A classification of the flow regimes at different Reynolds numbers is given in table 5.1.

5.2.2 Forces acting on a particle or droplet in a flow

A particle in a uniform flow field (meaning there is no acceleration) has many forces acting on it. In the direction of the flow is the "steady-state" drag force,F_D, further described later in this section. In upward direction the buoyancy force, F_B, due to the pressure gradient over the particle is equal to the weight of the fluid displaced, and works upwards from the surface. This force works in the same direction as the lift forces, F_L. The lift forces can be divided into the Saffmann lift, due to the velocity gradient near the wall, and the Magnus lift, which is the lift due to the rotation of the particle causing a velocity difference and pressure difference between the sides of the particle [44]. The adhesion forces, F_A, are the forces acting between the particle and the surface and works in downward direction. Adhesion forces can be divided into three types: van der Waals forces, electrostatic forces and capillary forces. If there is liquid present so that a liquid bridge can occur between the particle and the surface, capillary forces can be expected to be the largest contribution to the adhesion force [45]. The adhesion forces works in the same direction as the force due to gravity, F_G. Additionally, there is an external moment of surface stresses, M_D, acting through the center of the particle [9].

These forces are illustrated in figure 5.1.

Steady-state drag forces

The "steady-state" drag is the drag force which acts on the particle or droplet in a flow field when there is no acceleration of the relative velocity between the particle and the conveying fluid. The magnitude of this drag force depends on the characteristics of the flow, the size and shape of the particle, as well its orientation with respect to the flow

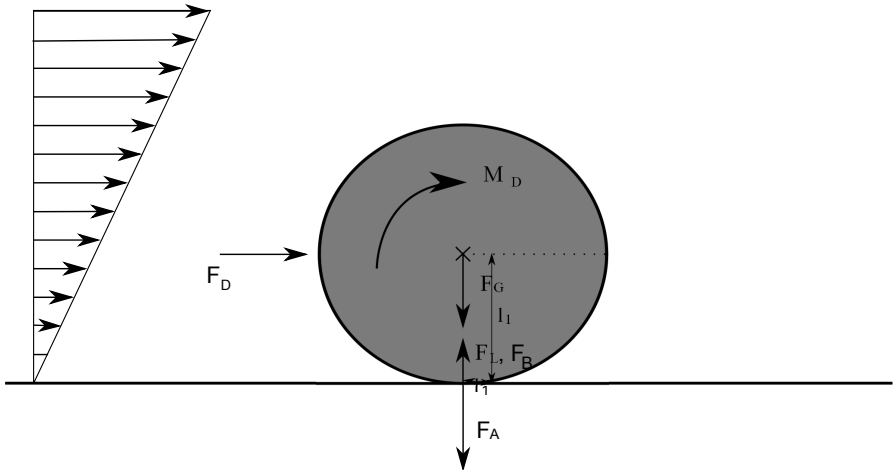

Figure 5.1: Forces acting on a smooth, deformable, spherical particle in a flow adhering to a smooth surface.

[44]. It can be quantified by the drag coefficient through the equation

$$F_D = \frac{1}{2}\rho_c C_D A \left|u - v\right| (u - v) \tag{5.1}$$

where ρ_c is the density of the continuous phase, C_D is the drag coefficient, A is the representative area of the droplet. In the special case where the particle is attached to a stationary surface, the expression is reduced to

$$F_D = \frac{1}{2}\rho_c C_D A u^2 \tag{5.2}$$

The drag coefficient will in general depend on the particle shape and orientation with respect to the flow, as well as on the flow parameters such as the earlier described Reynolds number, turbulence level and so on. The relationship between drag coefficient and Reynolds number can be found in table 5.1.

Flow regime	Reynolds number	Drag coeff.
Stokes	$\mathrm{Re} \leq 1$	$C_D = \frac{24}{Re}$
Transition	$1 \leq \mathrm{Re} \leq 1000$	$C_D = \frac{24}{Re}(1 + \frac{Re^{\frac{2}{3}}}{6})$
Newton Law	$1000 \leq \mathrm{Re} < 2 * 10^5$	$C_D = 0.44$

Table 5.1: Relationship between drag coefficient and Reynolds number [46].

Capillary forces

If there is humidity present in the system, it can condensate on the particle and surface and form a liquid surface joining the two, called a "bridge". This bridge is another consequence of the surface tension described in section 4.2.1.

If the liquid is pulled more by the particle than the surrounding fluid, the bridge will be curved as illustrated in figure 5.2. A curved interface implies a pressure difference on the sides of the interface.

A capillary bridge contributes with two forces: One is the adhesion forces due to the pressure difference across the curved surface and the other is the vertical component of the surface tension forces acting tangentially to the interface along the contact line [45].

The pressure difference can be quantified by the Young-Laplace equation [27]:

$$\Delta p = \gamma(\frac{1}{r^{'}} - \frac{1}{r^{''}} \approx \frac{\gamma}{r^{'}})(since r^{''} \gg r^{'}) \tag{5.3}$$

where Δp is the pressure difference across the fluid interface, γ is the interfacial tension between the two liquid phases, $r^{'}$ and $r^{''}$ are the principal radii of curvature, as shown in figure 5.2

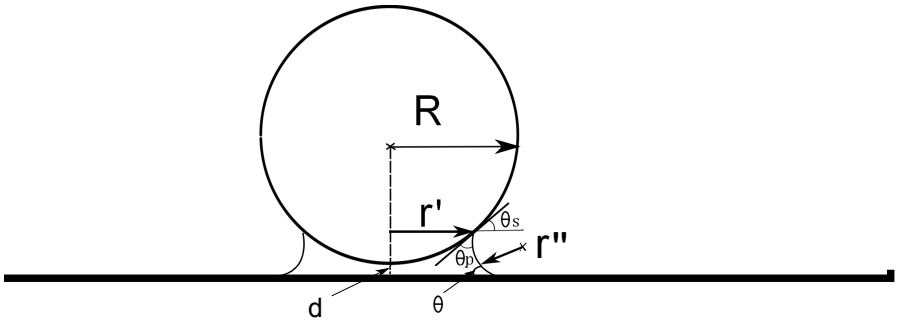

Figure 5.2: Capillary bridge between a particle and a surface.

The Laplace pressure acts on an area $\pi x^2 = 2\pi Rd$ between the two surfaces, pulling them together with a force $F \approx 2\pi Rd(\frac{\gamma}{r^{'}})$. If the contact area is small, the Laplace contribution to the adhesion force can be written [27]:

$$F_A \approx 4\pi R\gamma cos\theta \tag{5.4}$$

The other contributing force, arising from the surface tension along the contact line, can be expressed by [45]:

$$F_S = 2\pi r^{'}\gamma sin(\theta_p + \theta_s) \tag{5.5}$$

Unlike equation 5.4 which is subject to approximations, equation 5.5 is mathematically exact [45]. The total capillary force can be written:

$$F \approx 4\pi R\gamma cos\theta + 2\pi r^{'}\gamma sin(\theta_p + \theta_s) \tag{5.6}$$

θ_p is the contact angles and θ_s is the slope of the probe's contour at the contact line as shown in figure 5.2. It has been suggested that capillary forces are the explanation for the change in adhesion with increasing temperature often found in experiments on hydrates. A trend of increasing adhesive force with increasing temperature, was found by many researches ([9, 33, 34, 47]), while the opposite was found by Groysman et al.

[37]. This makes it relevant to study the attachment of liquid droplets to various solid surfaces, and the interfacial energies between the liquids and the wall materials, as is done in the following chapter.

The concept of capillary force between hydrate particles and between hydrate particles and pipeline walls has been a subject to research [33, 40, 48] and it has been suggested that the use of dry hydrates considerably reduce hydrate particle adhesion and hence agglomeration an a deposition [48].

5.2.3 Particle removal

There are three potential mechanisms for particle removal: lifting, sliding and rolling.

Lifting occurs when the lift forces and the buoyancy force are greater than the forces between the particle and the surface and the force due to gravity, and the particle is removed in the vertical direction:

$$F_L + F_B \geq F_A + F_G \tag{5.7}$$

,

By taking the force balance in the horizontal direction, one finds that sliding occurs when the drag force is larger than the frictional force:

$$F_D \geq \mu(|F_A| + F_G - F_L - F_B) \tag{5.8}$$

where μ is the static friction coefficient.

The criterion for rolling is:

$$M_D + F_D \cdot l_1 + F_L \cdot l_2 + F_B \cdot l_2 \geq F_A \cdot l_2 + F_G \cdot l_2 \tag{5.9}$$

where l_1 is the vertical distance between the drag force vector and the point around which rolling occurs, and l_2 is the horizontal distance between the lift and adhesion force vectors. This is illustrated in figure 5.1 in section 5.2.2. Note that the surface is considered smooth and the particle is considered spherical, smooth and deformable.

It has been found that rolling is the controlling mechanism of the three [42], which makes equation 5.9 the governing equation for these experiments.

5.3 Experimental

A setup was made to investigate the influence of flow on adhesion forces of a droplet or a particle.

5.3.1 The setup with the stirrer and container

These experiments was performed in a circular glass cuvette. A circular container was chosen because the flow pattern created is easier to simulate than for other geometries. The downside was that the visibility through the curved glass was inadequate, making

it impossible to take pictures through the glass. The motor used for the stirrer was a VWR VOS Power control with step less speed control from 0 to 2000 rpm, described in section 3.4.3.

There are two types of stirrers; those that generate radial flow and those that generate axial flow [49]. Radial flow is tangential to the impeller shaft, while the axial flow is parallel with the shaft. This experiment is performed with a liquid with low viscosity and vigorous stirring was needed; a stirrer which generate axial flow was chosen. The stirrer is from IKA, model R1311, described in section 3.4.4.

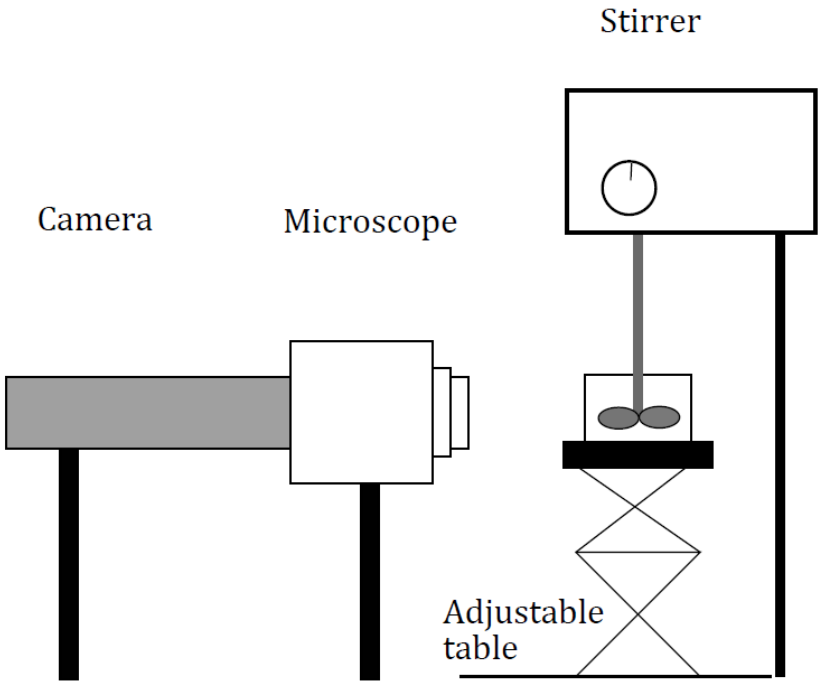

Figure 5.3: The setup with the microscope, camera and stirrer. The table was adjustable to make is easier to focus the microscope.

The diameter of the container should be approximately three times the diameter of the stirrer to obtain the right flow pattern. The height and the diameter should be approximately the same [49]. A twist lid with a hole for the stirrer was used to prevent spilling and evaporation.

In a circular container there will be some circular flow, regardless of the impeller type, meaning the liquid moves together with the impeller, so that less power is transferred from the stirrer to the liquid. Also the vortex created around the axis can cause problems, for example air bubbles. The circulation may be prevented by installing baffles.

Baffles will interfere the circulation, but not the radial or longitudinal flow. Since the container used was quite small, four baffles were used. The width of the baffles should be around one-twelfth of the tank diameter. A sketch can be seen in figure 5.4.

A container with diameter 9.5 cm was chosen and four baffles, 1 cm deep and 0.1 cm wide, were installed.

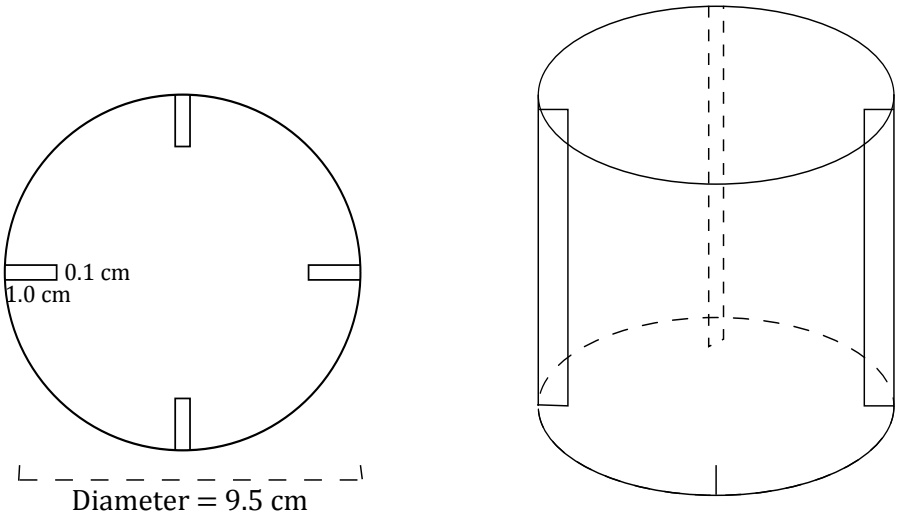

Figure 5.4: A sketch of the circular cuvette with four baffles.

Another problem was how to attach the surfaces and the baffles to the floor of the circular container. The plates had to be easily switchable, even when the container was filled with petroleum ether, to save time and chemicals, but not fall of when exposed to the flow field. An air hardening clay (Das Pronto Air Hardening Clay) was fitted to the bottom of the container and a hole was made to fit the plates. Since the clay does not harden when not exposed to air, the plates and baffles could be pressed into the clay and stand there.

To make sure that the clay did not interfere with the oil phase, an infrared spectroscopy was performed. The clay stayed in the petroleum ether for three hours before the sample was analyzed. No contamination of clay was found. More about the infrared spectroscopy can be found in the appendix, in section D.

A sketch of the whole setup can be seen in picture 5.3.

5.3.2 Making of hydrates

15 wt% TBAB brine (see section 3.1.1) was placed on a stirrer in a climat chamber at 2 °C to make a batch of hydrates.

When hydrates were grown on a surface, a droplet of 15 wt% TBAB brine was deposited onto the surface and a crystal from the batch was placed in the droplet to initiate growth.

This work distinguishes between "dry" and "wet" hydrates. This is because, in making a batch of hydrate, not all water was converted into hydrate. It was tried to change the concentration of TBAB, different temperatures, growth time and rate on stirring during growth, but it was found challenging.

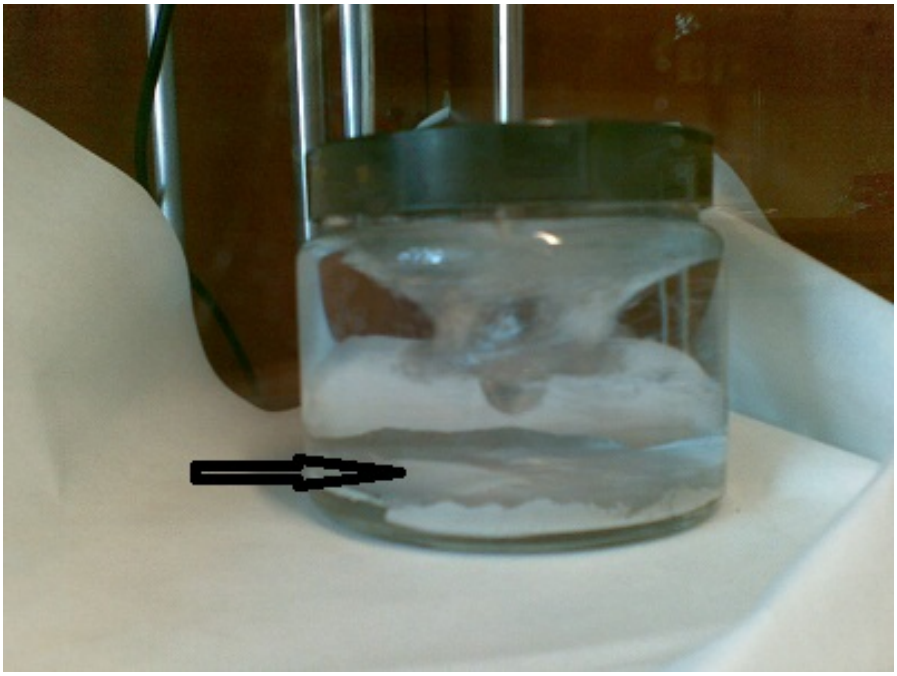

Figure 5.5: The clay used to attach the plates to the bottom of the container. The arrow is pointing to the epoxy surface.

5.3.3 Stirring procedure

The droplet or particle was placed on the surface which was placed in the middle between the container wall and center. In the initial experiments with the brine droplet and the hydrates grown on the surface, the speed was increased with 200 rpm every 30 second. The motor was turned off between every increase in stirring rate to observe the droplet. In the experiments with the deposited hydrate particle, the stirring rate was increased with 25 rpm every 30 second to make the results more precise. The motor was not turned off between every increase. The droplet was visually observed. Maximum speed of the stirrer was 2000 rpm.

5.3.4 Computational Fluid Dynamics

A Computational Fluid Dynamics (CFD) model was made and run in STAR-CD. CFD and STAR-CD are described in section 3.5. The model estimate the velocity of the fluid over the particle as a function of stirring rate. Screen shots from STAR-CD model can be seen in figure 5.7. Figure 5.8 shows a screen shot of the model after it is ran. The velocity vectors in the stirred beaker can be seen.

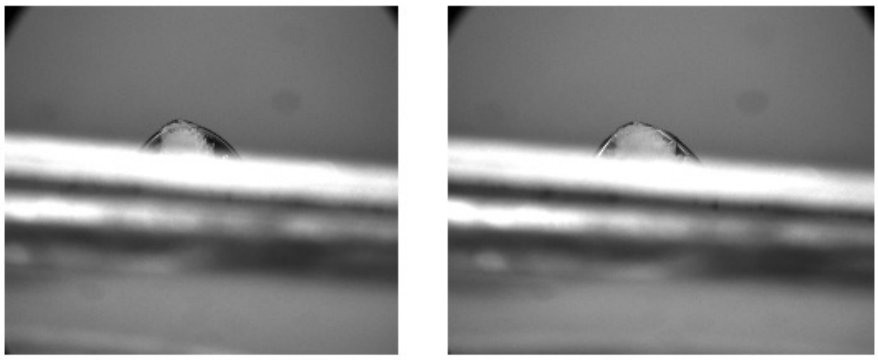

Figure 5.6: The picture shows hydrate growth on an aluminum surface. The left picture is right after the growth is initiated; the crystal that initiates the growth can be seen inside the droplet. The right picture is the same droplet, half an hour later. More brine is converted into hydrate.

5.4 Results

5.4.1 Water with hydrate former

A droplet of water with 15 wt% TBAB was dropped onto a surface and detached by a flow field created by a stirrer. The volume of the droplet was found by measuring the volume of ten droplets; $1,8 \cdot 10^{-3}$ ml. The experiment was performed at ambient temperature.

The results are presented in table 5.2 and figure 5.10, and the whole data set can be found in the appendix, in section B.1.

Surface	Stirring rate [rpm]	Re in cuvette
Glass	429 ± 70	15000
Steel	431 ± 72	15000
Aluminum	500 ± 82	17000
Brass	414 ± 45	14000
Epoxy	180 ± 108	6000

Table 5.2: The stirring rate needed to detach water droplets with 15w% TBAB from different surfaces in the presence of petroleum ether.

It was observed that when the volume of the water drops was large the drop split at an initial stirring rate while the rest of the drop detached at a higher stirring rate.

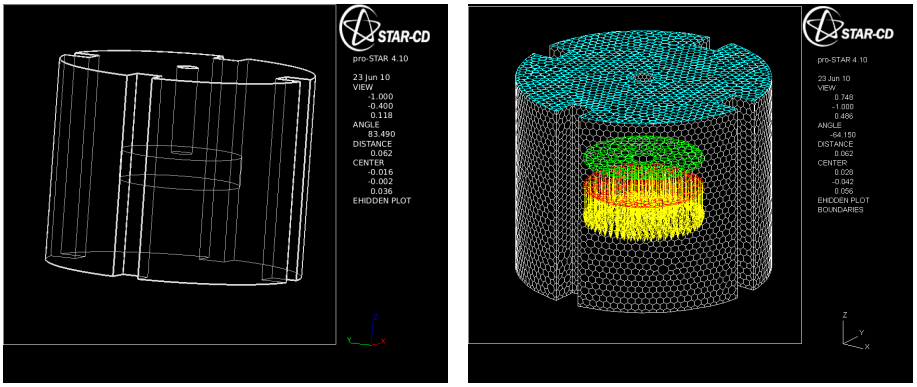

Figure 5.7: Screen shots of STAR-CD. The picture to the left shows the outline of the cuvette and the stirrer. The picture to the right shows boundary conditions with the downwards flow from the stirrer.

5.4.2 Hydrates grown on the surface

Without acid in the oil phase

A water droplet with 15 wt% TBAB was deposited onto a surface and a small hydrate particle of the same brine was injected to initiate growth as previously mentioned. The crystal was left to grow for 43.5 hours before stirring. The temperature was 2 °C, and the surfaces used were epoxy, brass and aluminum. These surfaces were chosen because it was found in chapter 4 that they have the lowest adhesion energy, and therefore a hydrate particle will probably adhere less to those compared to the other surfaces.

The hydrate particle did not detach from any of the surfaces, even at the maximum stirring rate, 2000 rpm. The same experiment was repeated with only one hour growth time and longer stirring time, but none of the hydrate particles detached.

With acid in the oil phase

Since acids are found to lower adhesion forces [12], similar experiments to those previously described were performed, but with naphtenic acid added to the oil phase. A hydrate was grown on an epoxy surface. Epoxy was chosen because it was found in chapter 4 that this was the surface with lowest adhesion energy, meaning that if the hydrate adhered too strongly to the epoxy surface to detach, it would not detach from any of the other surfaces either. The experiment was performed in four different procedures: with 1500 ppm or 5000 ppm added naphtenic acid and with 21 hours or 1 hour growth time. The hydrate did not detach in any of these systems, even at maximum stirring rate.

5.4.3 Hydrates deposited onto a surface

A premade hydrate particles of water with 15 wt% TBAB was deposited onto a surface, then detached using a flow field. The difference between ”wet” and ”dry” hydrates is

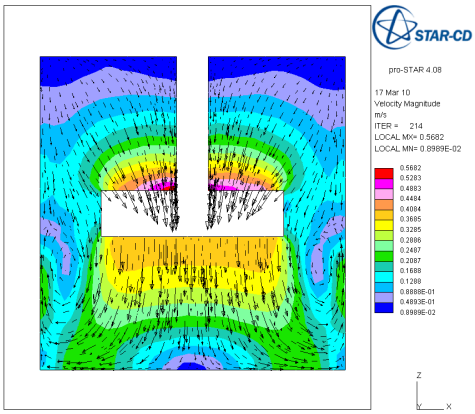

Figure 5.8: Screen shots of STAR-CD. The picture shows the velocity vectors at a random chosen stirring rate.

described in section 5.3.2.

Dry hydrates

Some preliminary experiments were performed where hydrates were deposited onto epoxy, aluminum and brass surfaces, and detached by a flow field. The temperature was -2 °C and the hydrates were left to settle for 44 hours. Both the hydrates on the epoxy and the aluminum surface detached at stirring rates too low to measure. The hydrate at the brass surface detached at 800 rpm.

Wet hydrates

Wet hydrates were deposited onto different surfaces and detached by a flowing fluid. The results can be found in table 5.3 and figure 5.10. The velocity over the particle was found by using a Computational Fluid Dynamics (CFD) model made in the simulation software STAR-CD. The particles were considered spherical, so that the projected area used as input in formula 5.1 was $\frac{\pi d^2}{4}$. The particle size was estimated to a diameter of 4 mm. Note that these experiments were performed in a different, larger, cuvette than the other experiments, so that the results are not comparable. Also, the climate chamber was partly broken and difficult to control, so there were some difference in the temperature in these experiments.

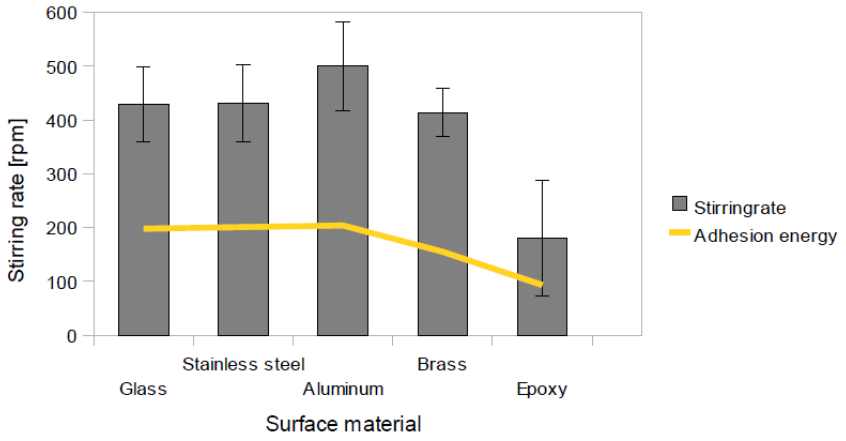

Figure 5.9: The graph shows at which stirring rate a droplet detaches from the different surface materials. The line represents the adhesion energy between the droplet and the surface found in chapter 4.

Surface	Temperature [°] C	Stirring rate [rpm]	Velocity [m/s]	Re in cuvette	Drag Force F_D [mN]
Glass	0-1	222 ± 17	0.083	17000	0.013
	2-3	240 ± 51	0.089	18000	0.015
Stainless steel	3-4	138 ± 12	0.052	11000	0.005
Aluminum	0-1	147 ± 59	0.055	1100	0.006
Brass	2-3	112 ± 11	0.042	9000	0.003
Epoxy	0-1	128 ± 30	0.049	10000	0.003

Table 5.3: The adhesion energy between a hydrate particle with 15 wt% TBAB and different surfaces in the presence of petroleum ether. The complete data set for the detach stirring rates can be found in the appendix, in section B.2.

5.5 Discussion

5.5.1 Water with hydrate former

The brine droplets detached from all surfaces in question, and the stirring rate needed to detach the droplet correlates with the adhesion energy calculated from the contact angles in chapter 4. This correlation is shown in figure 5.10. The stirring rate needed to detach the droplet from an aluminum surface was expected to be smaller to follow the trend of the adhesion energy. The stirring rate needed to detach the droplet from epoxy was significantly lower than the other surfaces, as expected from the adhesion.

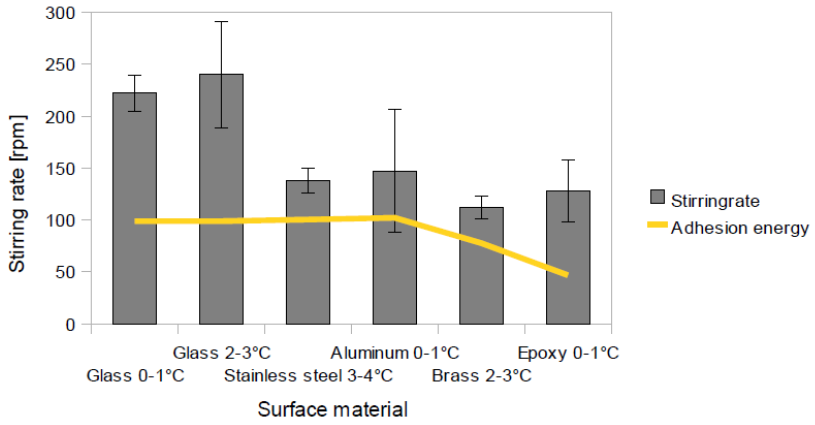

Figure 5.10: The graph represents at which stirring rate a wet hydrate detaches from the different surface materials. The line represents the adhesion energy between the droplet and the surface found in chapter 4.

5.5.2 Hydrates grown on a surface

A hydrate grown from a droplet deposited on a surface, did not detach from any of the materials investigated. As mentioned, acids have been found to lower the adhesion force; it would be expected that acid added to the oil phase would make the hydrate detach at a lower stirring rate, but the particles did not detach. This indicates that when a hydrate is first formed and attached to the pipeline wall, it will remain attached. One possible explanation may be that a liquid bridge is formed between the particle and the surface attaching the particle by capillary forces, described in section 5.2.2. A subsequent freezing of this bridge may form a solid bridge that anchors the hydrate to the surface very strongly. Variations in temperature may be an important factor.

These results correlate with results found by other authors [9, 37, 40], namely that a hydrate particle grown from a droplet deposited on the surface adheres strongly to the surface, and may stay there, independent of the flow characteristics.

5.5.3 Hydrates deposited onto a surface

Dry hydrates

In preliminary experiments, it was found that dry hydrates deposited onto a surface adhered very poorly. The stirring rates at which the particles detached were too low to measure, for both the epoxy and the aluminum surface. This indicates that the forces attaching a dry hydrate to a surface are very small.

One parallel was made in this experiment. The brass surface deviated from the aluminum and the epoxy surface (800 rpm compared to close to 0 rpm), and the explanation

for this may be that a layer of the hydrate melted when it was taken out from the batch, either from change in the surrounding temperature or heat from friction with the tool used to scrape it loose from the batch. When this layer froze again it possibly anchored the hydrate to the surface, analog to what happens when a hydrate is grown from a droplet on the surface.

Wet hydrates

The experiments with wet hydrates deposited on a surface shows that the stirring rate needed to detach the particle follows the same trend as the adhesion energy calculated in chapter 4. It is also found the the Reynolds number at at which a wet hydrate particle detaches from a surface, presented in table 5.2, are of the same order of magnitude as the Reynolds number at which droplet of brine detaches. This may indicate that a liquid bridge gives rice to capillary forces, as described in section 5.2.2, and that this is the governing adhesion mechanism.

Note that there is some difference in temperature between the experiments with the different surface materials. This is because the temperature in the climate chamber was difficult to control. There seems to be no correlation between temperature and deviation.

Two data sets with different temperatures were made for the glass surface. It was found that if the temperature is increased, an increased stirring rate is needed to detach the particle. But in general, temperatures does not seem to be the explanation when the detach stirring rate do not follow the adhesion energy as expected. For example epoxy has a higher stirring rate than expected, and a low temperature compared to the other experiments. To a certain point, higher temperature correlates with an even higher stirring rate needed to detach the particle. This is according to both the results performed on the glass surface and findings from other researchers ([9, 33, 34]).

A discussion around the calculated drag force can be found in chapter 6.

5.5.4 Possible explanations for deviations in the results

The calculated standard deviations in the experiments with detaching a liquid droplet and a wet particle are quite large. There can be many explanations for this, most probable are that the droplets or particles were not placed at the same distance from the stirrer, or that the size of the particles varied. For the experiments with the droplets, it was sometimes difficult to see if the droplet was detached or only split. Other possible explanations may be if the surfaces were not totally plane or totally clean. Surface roughness, both of the solid surface, as previously described, and on the particle, is also a possible reason. The uncertainty could possibly be reduced by controlling the size and position of the particle more accurately, but that would require other equipment used here.

5.5.5 Comparison between the Reynolds numbers

Table 5.11 show a comparison between the Reynolds numbers in the cuvette needed to detach brine in different phases from different surfaces. The line for hydrates grown on

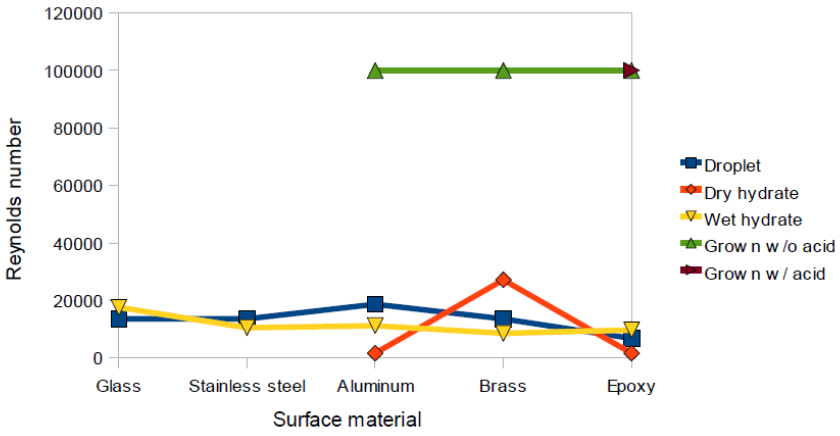

Figure 5.11: Comparison between the Reynolds numbers needed to detach 15 wt% TBAB brine in different phases.

a surface, both with and without acid, is chosen arbitrarily to indicate that the force needed to detach these hydrates are very high. In the experiments, none of the hydrates did detach.

The Reynolds numbers for wet hydrates and liquid droplet are very close to each other. This supports the theory that a force from the liquid bridge and thus capillary forces are the governing forces between a wet hydrate and surface.

5.6 Conclusion

The stirred beaker setup was developed to easily obtain a large dataset about the influence of flow on hydrate particles deposited on different surfaces. Usually, flow experiments involves a flow loop, in which changing the surfaces would be difficult and time consuming. In that matter, the setup lived up to its expectations. Regardless, some improvements could have made the experimental data applicable. A better temperature control would have made it easier to investigate the effect of temperature. Better visibility could make is possible to acquire pictures could be taken of the droplets would have made it possible to investigate the effect of particle size.

It was found that wetting properties do influence the forces between hydrates or liquid droplets and solid surfaces. A brine droplet or a hydrate particle deposited onto a surface may be detached from the surface, and the force needed to detach is different for different surfaces. A surface with higher adhesion energy require a higher flow rate for the droplet or particle to detach. A dry hydrate particle will adhere to the wall with

very little force, which indicates that a flow with no or little unbound water may have a low plugging tendency. A wet hydrate, on the other hand, will stick to the wall, but detach under right conditions. The similar Reynolds numbers needed to detach a wet hydrate and a may indicate that capillary forces are the governing forces between a wet hydrate and a surface. A hydrate grown from a water droplet on the wall will possibly "anchor" to the surface and stay there.

5.6.1 Further work

Suggestions for further work would be to do the experiments with different additives, such as acids, to see how the adhesion forces changes. It would also be interesting to investigate the effect of temperature and droplet or particle size more thoroughly.

Chapter 6

Dynamic contact angles of droplets in a flow field

A liquid droplet sitting on a surface in a flowing fluid will be swept away if the velocity of the fluid is high enough. Because of the forces between the droplet and the surface, a droplet that experiences a pull-of force will be deformed before it dislodges. The change in the contact angles can be used together with the the interfacial tension to find the adhesion force between the droplet and the surface.

6.1 Background and literature survey

The purpose of this experiment is to calculate the force needed to detach a droplet.

Shen et al. [50] used a drive electrode placed next to a mercury droplet to pull or lift it off a surface. They measured the change in the angles on the droplet and the pulling force to find the surface tension. The force exerted by the drive electrode works in the same direction as the drag force exerted by a flowing fluid and these forces are analog to each other. Shen et al. presented an algorithm to find the force needed to "detach" (force acting perpendicular to the surface) or "slide" (force acting parallel to the surface) a liquid droplet off a surface. The force is given in terms of the surface tension between the droplet and the surrounding medium, the contact ratio between the droplet and the surface, and the angles of the droplets in the instant before it slides or detaches. This algorithm is rewritten and used to calculate the force needed to dislodge a droplet in a flowing fluid.

An overview of forces working on a particle or droplet in a flowing fluid can be found in chapter 5.

6.2 Theoretical Background

When a droplet is exposed to a flow, the shape will change to restore equilibrium. The angle closest to the flow will become lower, the other higher. These angles are called

the dynamic contact angles of the droplet [41], in contrast to the static contact angles measured in chapter 4. The dynamic contact angles, measured when the velocity of the flowing fluid is large enough to dislodge the droplet, can be used to find the force between the droplet and the surfaces. Shen et al. [50] found that this force can be expressed as:

$$F_dis = \gamma Lcos(\pi - \theta_{adv}) - \gamma Lcos(\pi - \theta_{rec}) \tag{6.1}$$

where θ_{adv} and θ_{rec} is the advancing and receding contact angle, γ is the droplet/surrounding media surface tension and L is the contact length between the droplet and solid surface. W. Shen et al. expresses the contact length in terms of the radius of the droplet and and the static contact angle. In this work, it is expressed as explained in section 6.2.1

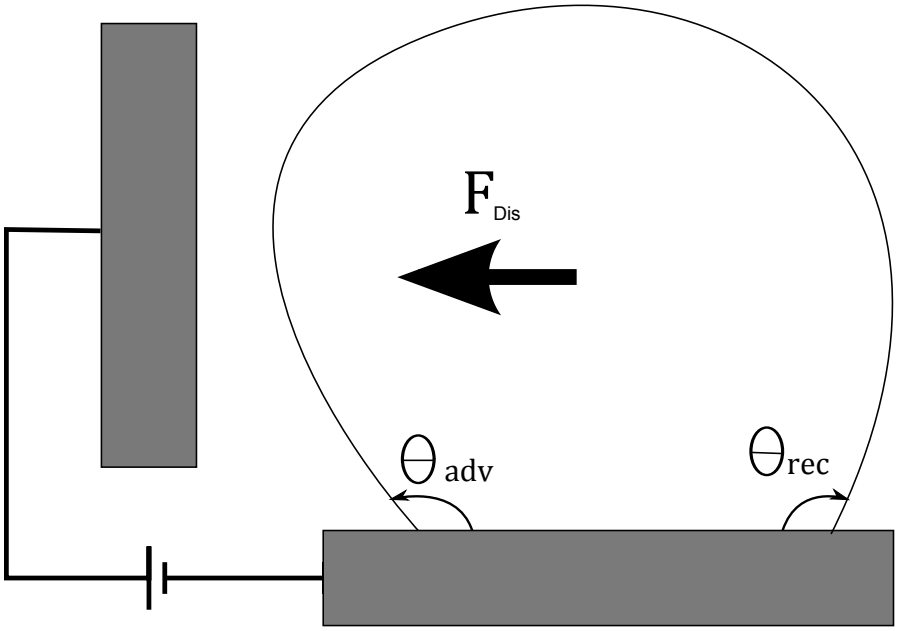

Figure 6.1: The modified picture from the article written by Shen et al. [50] shows the droplet sliding on the surface. The advancing angle is the angle that becomes higher when exposed to the flow, the receding angle is the angle that becomes lower. On the left side is the drive electrode they used to detach the droplet.

6.2.1 Calculating the contact length

The length of the contact line between the droplet and the surface, called the contact length, is the circumference

A droplet sitting on a surface can be taken as a cap of a sphere [51]; the volume of the droplet equals the volume of the cap as illustrated in figure 6.2. The volume of a sphere cap can be expressed by equation 6.2

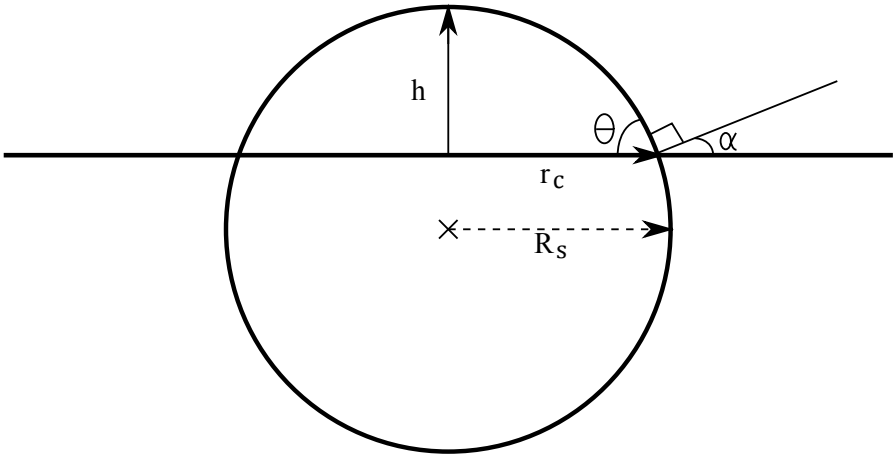

Figure 6.2: A droplet sitting on a surface can be seen as a part of a sphere.

$$V_{cap} = \frac{1}{3}\pi R_s^3(2 - 3sin\alpha + sin^3\alpha) \tag{6.2}$$

where R_s is the radius of the sphere and α is the angle between the normal to the sphere at the bottom of the cap and the base plane. The relationship between α and the static contact angle θ straightforward and illustrated in figure 6.2. Once α is found, R_s can be found by iteration, and equation 6.3 can be used to find the height of the cap, h.

$$R_s - h = R_s sin\alpha \tag{6.3}$$

Another expression for the volume of the cap is

$$V_{cap} = \frac{1}{6}\pi h(3r_c^2 + h^2) \tag{6.4}$$

In equation 6.4 r_c is the only unknown. When r_c is found, finding the contact length is straight forward.

6.3 Experimental

A droplet of water with 15 wt% TBAB (see section 3.1.1) was deposited onto different surfaces in petroleum ether. The setup was the same as described in chapter 5, using a cubical cuvette to enable use of camera. The fluid was set in motion, and a live video was made of the droplet. When the stirring rate is constant, the droplets will deforme, making it possible to find the dynamic contact angles of the droplet. The angles were found by analyzing the image recorded right before dislodgement in the same way as for static contact angles, described in section 4.3. The process of capturing the dislodgement with the camera and the post processing of the live video was time consuming, however 3-4 parallels were made. A picture of a droplet during stirring can be seen in figure 6.3.

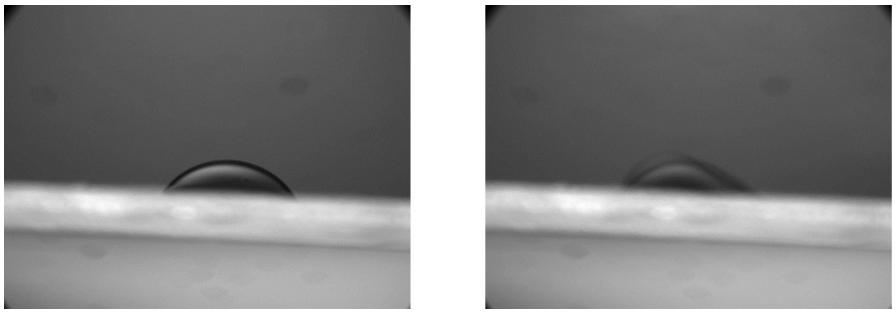

Figure 6.3: The picture shows water droplets sitting on an aluminum surface. The picture on the left hand side is before stirring, the picture on the right hand side shows the droplet during stirring, before it dislodges from the surface. The edge of the droplet is uneven because the droplet is oscillating slightly, due to the revolutions of the stirrer.

6.4 Results

The dynamic contact angles between a liquid droplet of 15 wt% TBAB brine and different surfaces in a flow of petroleum ether were measured and the force needed to dislodge the droplet was calculated. When a deposited droplet is exposed to a flow is first deformes, and when the velocity is high enough, the droplet "slides" of the surface and disappears. The dislodge force is calculated using the interfacial tension and the dynamic contact angles as input in equation 6.1. The interfacial tension between 15w% TBAB brine and petroleum ether was found in chapter 4 to be 10,71 mN/m.

Surface	Left angle (degrees)	Right angle (degrees)	Dislodge force [mN]
Glass	17 ± 1	15 ± 2	0.264
Steel	50 ± 9	19 ± 8	0.269
Aluminum	53 ± 18	31 ± 5	0.246
Brass	89 ± 7	75 ± 7	0.022
Epoxy	91 ± 11	75 ± 5	0.016

Table 6.1: Dynamic contact angles of 15 wt% TBAB brine on different surfaces, with corresponding dislodge forces.

Table 6.1 shows the angle of the droplet sitting on a surface on a flow field, in the moment before it dislodges, and the calculated force needed to dislodge it. The whole data set can be found in the appendix, in section C. The droplets all have the same volume; the only variables in the experiment are the material of the solid surface and the stirring speed.

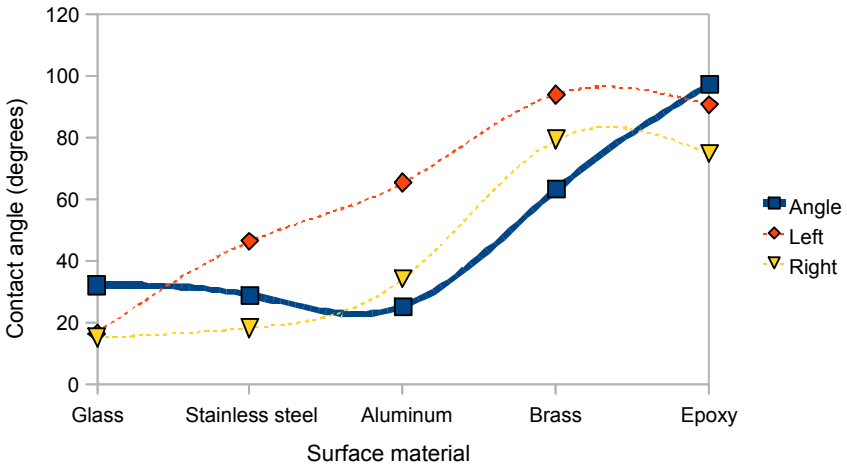

Figure 6.4: Comparison between the contact angles of water with 15 wt% TBAB on different surfaces: Static- and dynamic contact angles.

6.5 Discussion

The angles ordered from lowest to highest, do not strictly follow the trend of the static contact angles found in chapter 4, as illustrated in figure 6.4. The general trend, however, is the same. It can also be seen that the droplets with the lowest static contact angle have the least deformation, that is, the smallest difference between the receding and advancing contact angle.

The force needed to dislodge a droplet is calculated from equation 6.1, and shows the same trend as the calculated adhesion energies between a droplet and a surface calculated in chapter 4. Glass, stainless steel and aluminum shows almost the same properties, while brass and epoxy has a considerably lower adhesion energy and dislodge force.

Comparison between force needed to dislodge a droplet and a wet hydrate particle

Table 6.2 shows the force needed to dislodge a liquid particle of brine and the drag force needed to dislodge a wet hydrate particle, found in chapter 5. These forces are, as already mentioned, analog to each other.

It was found in chapter 5 that the Reynolds numbers of a flow needed to dislodge a droplet of brine and a wet hydrate deposited onto various surfaces, are in the same order of magnitude. It was concluded that the reason for this may be that a liquid bridge attaches the hydrate to the surface; the governing forces are the same for the two systems. The calculated forces shown in table 6.2, however, are not in the same order. The forces are also more spread (0.25 mN between the largest and smallest) than the drag forces on a wet hydrate found in chapter 5 (0.04 mN between the largest and

Surface	Dislodge force F_{Dis} droplet [mN]	Drag Force F_D wet hydrate [mN]
Glass	0.264	0.014
Stainless steel	0.269	0.005
Aluminum	0.246	0.006
Brass	0.022	0.003
Epoxy	0.016	0.003

Table 6.2: The table shows the force needed to dislodge a liquid droplet of brine, found in this chapter, and the drag force needed to dislodge a wet hydrate particle, found in chapter 5.

smallest).

The reason for this is probably in the simplifications made in the calculations. To calculate the drag force on the wet hydrate particles, the particles were considerer spherical, giving an estimate of the projected area that is larger than the area of the real particle. A correct projected area would give a smaller drag force. To calculate the force needed to dislodge a droplet, it was assumed that the surfaces were perfectly smooth, which gives a shorter contact length and thus a smaller calculated force.

Anyhow, the fact that the calculated forces to follow the same trend as the adhesion energy, indicates that the experimental setup of using a stirred beaker to measure the dynamic contact angles can be used to compare the different surfaces to each other.

6.6 Conclusion

A stirred beaker setup was used to find the dynamic contact angles of droplets of 15 wt% TBAB brine. The results were used to calculate the force needed to dislodge the droplet.

The calculated force followed the trend of the calculated adhesion force between a droplet of brine and the various surfaces. However, the dislodgement force was compared to the previously calculated drag force needed to detach a wet hydrate particle. They were expected to be in the same order of magnitude, but were not. The reason for this is probably the simplifications made in the calculations. Regardless, the fact that the force followed the trend of the adhesion energy, indicates that a stirred beaker and dynamic contact angles can be used to compare the surfaces, but a better algorithm is needed to quantify the forces.

Chapter 7

Conclusion

A stirred beaker setup that enables investigation of the effect of flow on hydrate deposition on various surfaces has been developed. The goal was to develop a setup the was simpler to use that the traditionally used flow loop. This was achieved; the setup lived up to its expectations, but has to be refined.

The static contact angles of brine of different surfaces were measured, and the results were used to calculate the adhesion energy. It was found that the epoxy surface is the only oil-wet surface, with a low adhesion energy. The brass surface is slightly water-wet, while glass, stainless steel and aluminum all have low contact angles, and corresponding high adhesion energy. This indicates that a water droplet will adhere less strongly to a epoxy surface, compared to the other surfaces in question.

Hydrates, in form of brine, hydrates grown on a surface and deposited hydrates, with and without acid in the oil phase, were tried detached from different surfaces, using the stirred beaker setup. A CFD model of the setup was used to determine the velocity of the fluid over the particle, and the drag force acting on the particle was calculated. It was found that the force needed to detach a water droplet and a deposited hydrate follows the trend of the calculated adhesion force between the solid surfaces and brine. It was also found that a hydrate grown on a surface adheres very strongly to the surface, while a deposited dry particle adhere very poorly. A wet hydrate, on the other hand, detaches at the same Reynolds number as a droplet of brine, which indicates that capillary forces are the governing adhesion mechanism.

The stirred beaker setup was used to measure the dynamic contact angles of droplets of brine on various surface. An algorithm was used to calculated the force needed to dislodge the droplets. This force followed the trend of the calculated adhesion force between brine and the solid surfaces. Since the Reynolds number needed to detach a water droplet and a wet hydrate with the stirred beaker was approximately the same, the calculated drag force on the wet hydrate and the force needed to dislodge the droplet were compared and expected to be of the same order of magnitude. This was not the case, the calculated force to dislodge the droplet was considerably smaller. The reason for this was probably the simplifications made when calculating the forces. However, the fact that the forces follows the trend, indicates that the experimental technique can

be used to compare surface materials, but to find the exact force, the algorithm has to be further developed.

Bibliography

[1] E.D.Sloan and C.A. Koh. *Chlatrate Hydrates of Natural Gases, 3.ed.* CRC Press, Golde, Colorado, U.S.A, 2008.

[2] E. G. Hammerschmidt. Formation of gas hydrates in natural gas transmission lines. *Industrial and Engineering Chemistry*, 26:151–155, 1934.

[3] G. D. Holder, V. A. Kamath, and S. P. Godbole. The potential of natural gas hydrates as an energy resource. *Annual Review of Energy*, 9:427–445, 1984.

[4] A. Demirbas. Methane hydrates as potential energy resource: Part 1: importance, resource and recovery facilities. *Energy Conversion and Management*, 51:1547–1561, 2010.

[5] G. J. Moridis. Toward production from gas hydrates: Current status, assessment of resources, and simulation-based evaluation of technology and potential. *SPE Reservoir Evaluation & Engineering*, 12:745–771, 2009.

[6] E. D. Sloan. Clathrate hydrates: The other common solid water phase. *Industrial and Engineering Chemistry Research*, 39:3123–3129, 2000.

[7] J. Carroll. *Natural Gas Hydrates, A Guide for Engineers, 2.ed.* Gulf Professional Publishing, 2009.

[8] M. N. Lingelem, A. I. Majeed, and E. Stange. Industrial experience in evaluation of hydrate formation, inhibition, and dissociation in pipeline design and operation. *Proceedings of International Conference on Natural Gas Hydrates*, 715:75–93, 1994.

[9] J. W. Nicholas, L. E. Dieker, L. Nuebling, B. Horn, H. He, C. A. Koh, and E. Dendy Sloan. Experimental investiation of deposition and wall growth in water saturated hydracarbon pipelines in th eabsence of free water. *Proceedings of the 6th International Conference on Gas Hydrates (ICGH 2008)*, 0:1–2, 2008.

[10] M. R. Anklam, J. D. York, L. Helmerich, and A. Firoozabadi. Effects of antiagglomerants on the interactions between hydrate particles. *AIChE Journal*, 54:565–574, 2008.

[11] M. A. Kelland, T. M. Svartaas, and J. Øvsthus. A new class of kinetic hydrate inhibitor. In *Conferences, presented Oil Field Chemicals Symposium på Fagernes 28.02.99 - 03.03.99*, RF-Rogaland Research, Norway, 1999.

[12] G. Aspenes, S. Høiland, T.Barth, and K.M. Askvik. The influence of petroleum acids and solid surface energy on pipeline wettability in relation to hydrate deposition. *Journal of Colloid and Interface Science*, 2009.

[13] G. Aspenes. *The influence of pipeline wettability and crude oil composition on deposition of gas hydrates during petroleum production.* PhD thesis, University of Bergen, Norway, 2010.

[14] F. H. Fadnes. Natural hydrate inhibiting components in crude oils. *Fluid Phase Equilibria*, 117:189–192, 1996.

[15] S.Høiland, K.M. Askvik, P. Fotland, E. Alagic, T. Barth, and F. Fadnes. Wettability of freon hydrates in crude oil/brine emulsions. *Journal of Colloid and Interface Science*, 287:217–225, 2005.

[16] W. Shimada, M. Shiro, H. Konda, S. Takeya, H. Oyama, T. Ebinuma, and H. Narita. Tetra-a-butylammonium bromide - water. *International Union of Crystallography*, 61:65–66, 2005.

[17] Sigma-Aldrich. `http://www.sigmaaldrich.com`.

[18] H. Oyama, W. Shimada, T. Ebinuma, Y. Kamata, S. Takeya, T. Uchida, and H. Narita J. Nagao. Phase diagram, latent heat, and specific heat of tbab semi-clathrate hydrate crystals. *Fluid Phase Equilibria*, 234:131–135, 2005.

[19] Sigma-Aldrich. `http://www.sigmaaldrich.com/catalog/ProductDetail.do?lang=en&N4=32248|SIAL&N5=SEARCH_CONCAT_PNO|BRAND_KEY&F=SPEC`.

[20] Nikon. `http://www.nikon.com/products/instruments/lineup/stereoscopic_microscopes/smz800/index.html`.

[21] QImaging. `http://www.meyerinst.com/digital-cameras/qimaging/RetigaEXi_fast1394.pdf`.

[22] VWR. `http://no.vwr.com/app/catalog/Product?article_number=411-9213`.

[23] IKA. `http://www.ika.net`.

[24] Jr J. D. Anderson. *Computational Fluid Dynamics, The basics with applications.* McGraw-Hill, New York, 1995.

[25] F. Wenstop. *Statistikk og dataanalyse, 4. utgave.* Tano Aschehoug, 1997.

[26] R. G. dos Santos, R. S. Mohamed, A. C. Bannwart, and W. Loh. Contact angle measurements and wetting behavior of inner surfaces of pipelines exposed to heavy crude oil and water. *Journal of Petroleum Science and Engineering*, 51:9–16, 2006.

[27] J. Israelachvili. *Intermolecular & Surface Forces, 2.ed.* Academic Press, 1991.

[28] K. J. Laidler, J. H. Meiser, and B. C. Sanctuary. *Physical Chemistry, Fourth Edition.* Houghton Mifflin Company, Boston, New York, 2003.

[29] G. T. Barnes and I. R. Gentle. *Interfacial science, an introduction.* Oxford University Press, 2006.

[30] P. Atkins and J. de Paula. *Atkins´ Physical Chemistry, Eight Edition.* Oxford University Press, 2006.

[31] J. Campbell. Surface tension measurements by the drop weight technique. *Journal of physics, D: Applied Physics*, 1970.

[32] F. K. Skinner, Y. Rotenberg, and A. W. Neumann. Contact angle measurements from the contact diameter of sessile drops by means of a modified axisymmetric drop shape analysis. *Journal of colloid and interface science*, 130:25–34, 1989.

[33] S. Yang, D. M. Kleehammer, Z.Huo, E. D. Sloan, and K. T. Miller. Micromechanical measurements of hydrate particle attractive forces. In *Paper presented at 15th Symposium on Thermophysical Properties*, Colorado, 2003.

[34] C. J. Taylor, L. E. Dieker, K. T. Miller, C. A. Koh, and E.D. Sloan Jr. Micromechanical adheison force measurements between tetrahydrofuran hydrate particles. *Journal of Colloid and Interface Science*, 306:255–261, 2007.

[35] W. A. Ducker, T. J. Senden, and R. M. Pashley. Direct measurements of colloidal forces using an atomic force microscope. *Nature*, 353:239–241, 1991.

[36] T. Sugimoto, T. Takahashi, H. Itoh, S. Sato, and A. Muramatsu. Direct measurements of interparticle forces by the optical trapping technique. *Langmuir*, 13:5528–5530, 1997.

[37] A.G. Groysman and A.Z. Savvin. Adhesion properties of gas hydrates. *Natural and technological gas hydrates (collected articles), Moscow*, pages 84–93, 1990.

[38] G. Aspenes, L. E. Dieker, Z.M. Aman, S. Høiland, A.K. Sum, C.A. Koh, and E.D. Sloan. Adhesion force between cyclopentane hydrates and solid surface materials. *Journal of Colloid and Interface Science*, 343:529–536, 2009.

[39] H. Pedersen. Formation, particle size distribution and flow dependence of freon (r11) hydrates in multiphase flow systems. *Department of Physics and Technology, University of Bergen, Norway. Master thesis*, 2008.

[40] J. W. Nicholas, L. E. Dieker, E.D. Sloan, and C. A. Koh. Assessing the feasibility of hydrate deposition on pipeline walls - adhesion force measurementes of claturate hydrate particles on carbon steel. *Journal of Colloid and Interface Science*, 331:322–328, 2009.

[41] A. Theodorakakos, T. Ous, M. Gavaises, J. M. Nouri, N. Nikolopoulos, and H. Yanagihara. Dynamics of water droplets detached from porous surfaces of relevance to pem fuel cells. *Journal of Colloid and Interface Science*, 300:673–687, 2006.

[42] G. M. Burdick, N. S. Berman, and S. P. Beaudoin. Hydrodynamic particle removal from surfaces. *Thin Solid Films*, 488:116–123, 2005.

[43] G. Aspenes, B. Balakin, A. E. Borgund, and S. Hiland. Hydrate agglomeration and deposition studies - the influence of pipeline wettability and flow. In *Proceedings of Oil Field Chemistry Symposium (OFCS), Geilo, Norway*, Geilo, 2009.

[44] C. Crowe, M. Sommerfeld, and Y.Tsuji. *Multiphase Flows with Droplets and Particles*. CRC Press, Florida, 1998.

[45] A. de Lazzer, M. Dreyer, and H. J. Rath. Particle-surface capillary forces. *Langmuir*, 15:4551–4559, 1999.

[46] Cyberman Education. `www.mfg.mtu.edu/cyberman/environment/air/forces/forces.html`.

[47] S.O. Yang, D.M. Kleehammer, Z. Huo, E. D. Sloan, and K. T. Miller. Temperature dependence of particle-particle adherence forces in ice and clathrate hydrates. *Journal of Colloid and Interface Science*, 277:335–341, 2004.

[48] Jon Steinar Gudmundsson. Cold flow hydrate technology. In *4th International Conference on Gas Hydrates*, Yokohama, May 2002.

[49] W. L. McCabe, J. C. Smith, and P. Harriott. *Unit operations of chemical engineering, Seventh Edition*. McGraw-Hill, 'New York', 2005.

[50] W. Shen, J. Kim, and C.-J. "CJ" Kim. Controlling the adhesion force for electrostatic actuation of microscale mercury drop by physical surface modification. In *The Fifteenth IEEE International Conference on Micro Electro Mechanical Systems*, Los Angeles, 2002.

[51] Math World. `http://mathworld.wolfram.com/SphericalCap.html`.

[52] University of Colorado. Infrared spectroscopy: Theory. *Online edition for students of organic chemistry lab courses at the University of Colorado, Boulder, Dept of Chem and Biochem*, 2002.

[53] D. L. Pavia, G. M. Lampman, G. S. Kriz, and J. R. Vyvyan. *Introduction to Spectroscopy, Fourth Edition*. Brooks/Cole Cengage Learning, Belmont, USA, 2009.

Appendix A

Solid surface wetting properites

A.1 Images of droplets

Images of water droplets with 15 wt% TBAB on different solid surfaces at ambient temperature

A.1.1 Glass

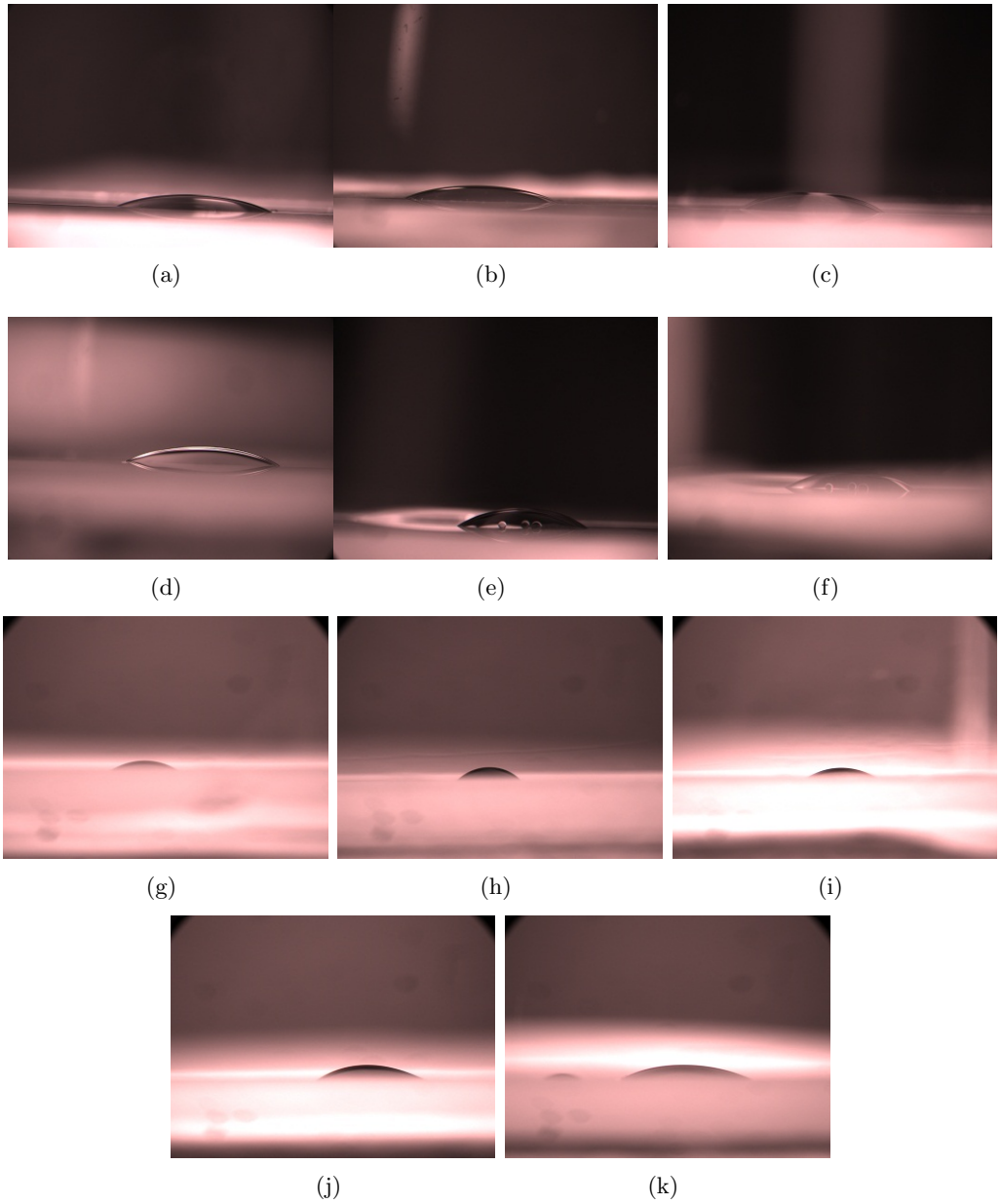

(a) (b) (c)

(d) (e) (f)

(g) (h) (i)

(j) (k)

Figure A.1: Images of brine on glass

A.1.2 Stainless steel

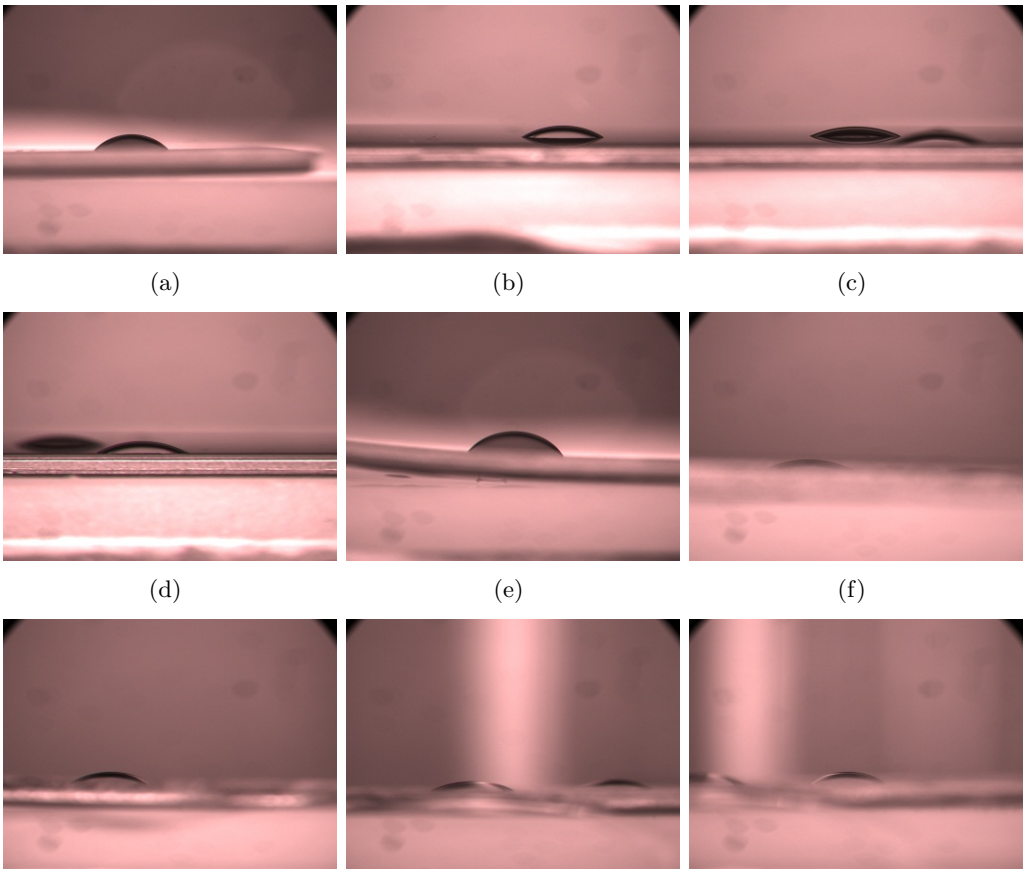

(a) (b) (c)

(d) (e) (f)

(g) (h) (i)

Figure A.2: Images of brine on stainless steel

A.1.3 Aluminum

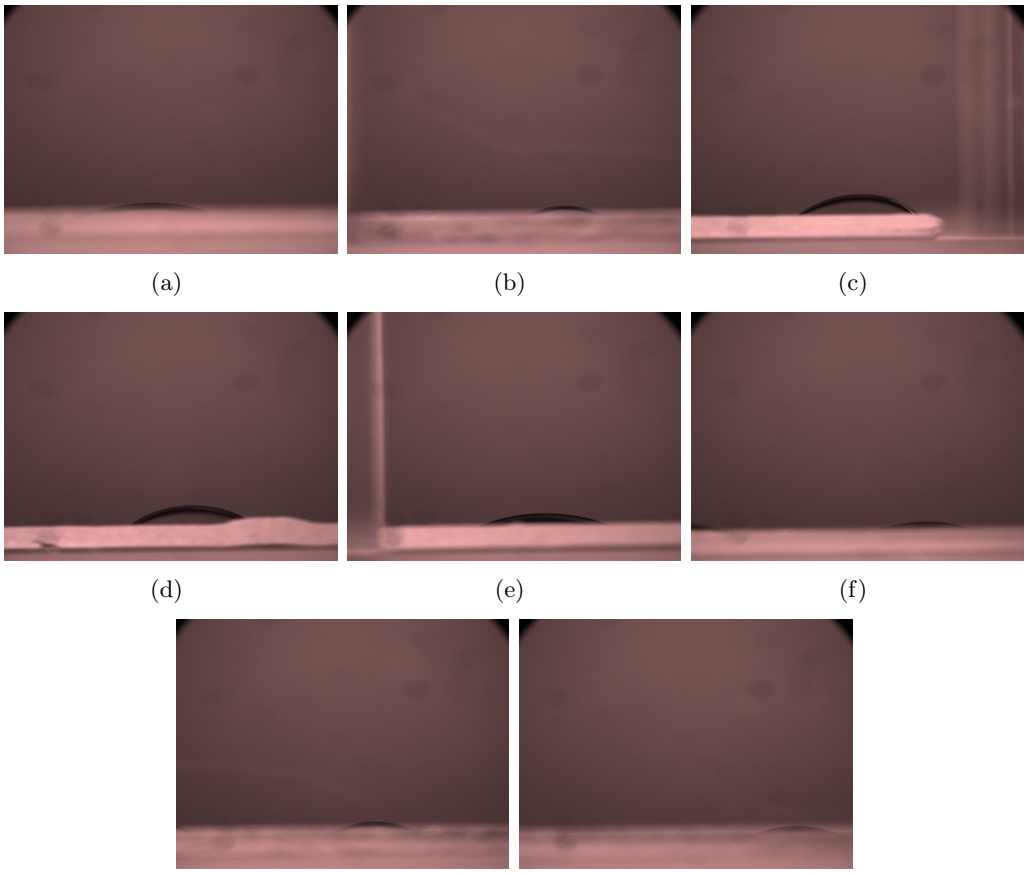

(a) (b) (c)

(d) (e) (f)

(g) (h)

Figure A.3: Images of brine on aluminum

A.1.4 Brass

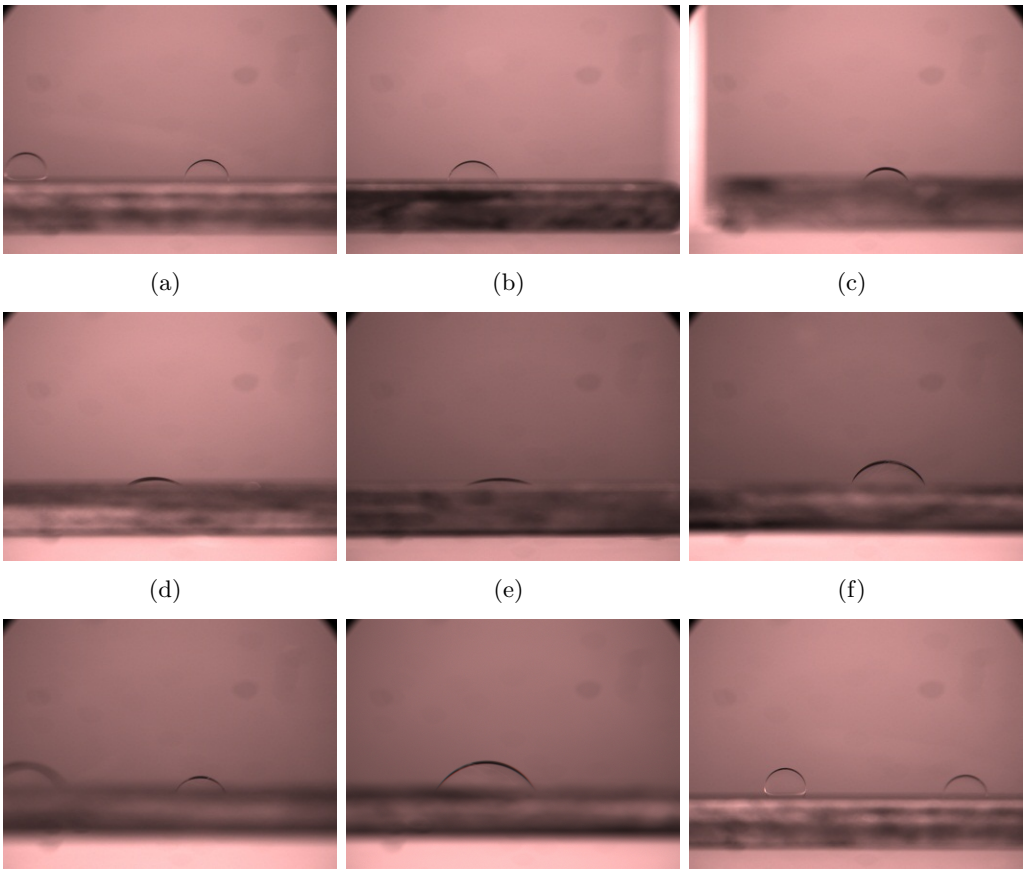

(a) (b) (c)

(d) (e) (f)

(g) (h) (i)

Figure A.4: Images of brine on brass

A.1.5 Epoxy

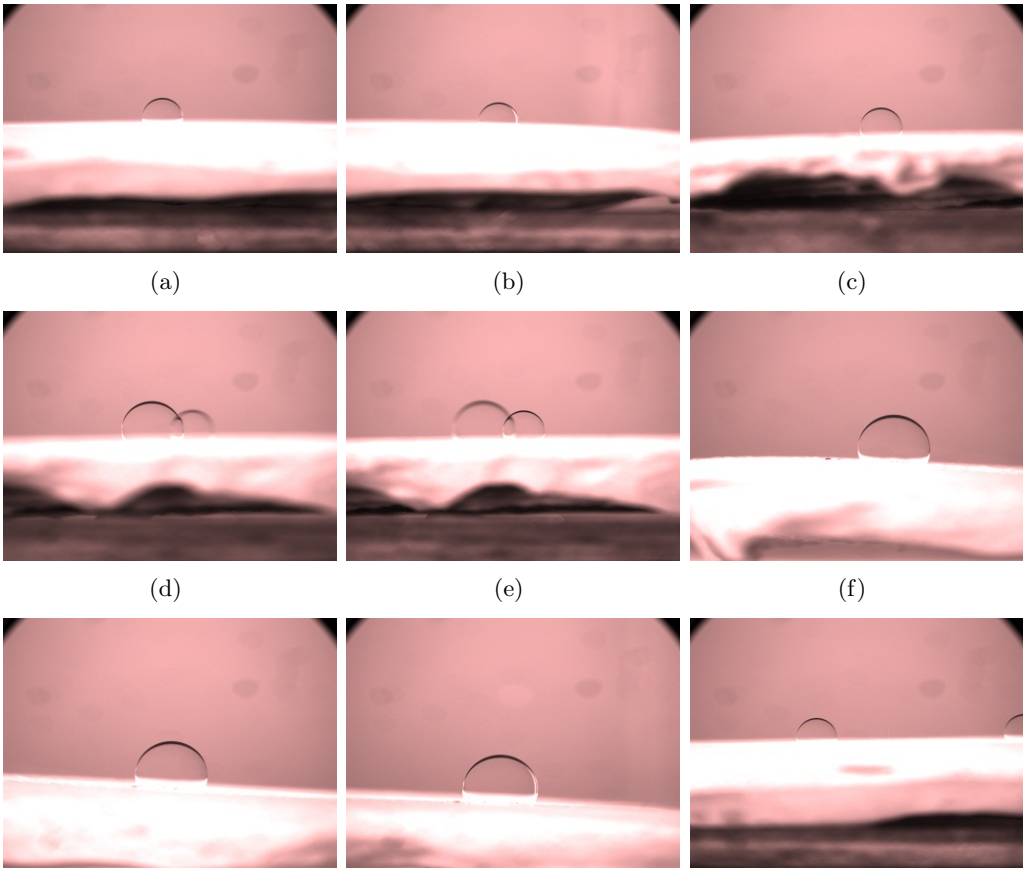

(a) (b) (c)

(d) (e) (f)

(g) (h) (i)

Figure A.5: Images of brine on epoxy

A.2 Contact angles of brine on different surfaces

Measured contact angles of water droplets with 15 wt% TBAB on different solid surfaces at ambient temperature

A.2.1 Glass

Measurement	Left angle (degrees)	Right angle (degrees)
Measurement 1	24.439	25.849
Measurement 2	23.176	23.482
Measurement 3	24.596	25.045
Measurement 4	21.947	22.777
Measurement 5	23.116	24.796
Mean	**23.5**	**24.4**
Standard deviation	0.97	1.11

Measurement	Left angle (degrees)	Right angle (degrees)
Measurement 1	23.116	28.609
Measurement 2	25.785	30.072
Measurement 3	31.676	27.042
Measurement 4	23.142	23.859
Measurement 5	24.624	22.793
Mean	**25.7**	**26.5**
Standard deviation	3.17	2.75

Measurement	Left angle (degrees)	Right angle (degrees)
Measurement 1	29.417	33.550
Measurement 2	35.895	29.340
Measurement 3	36.757	32.880
Measurement 4	33.686	32.503
Measurement 5	33.272	34.111
Mean	**33.8**	**32.5**
Standard deviation	2.55	1.66

Measurement	Left angle (degrees)	Right angle (degrees)
Measurement 1	22.639	29.777
Measurement 2	22.086	30.265
Measurement 3	22.958	32.089
Measurement 4	22.779	31.597
Measurement 5	20.494	31.063
Mean	**22.2**	**31.0**
Standard deviation	0.90	0.85

Measurement	Left angle (degrees)	Right angle (degrees)
Measurement 1	29.086	32.207
Measurement 2	29.226	34.548
Measurement 3	31.766	35.699
Measurement 4	29.511	36.800
Measurement 5	31.589	35.627
Mean	**30.2**	**35.0**
Standard deviation	1.19	1.56

Measurement	Left angle (degrees)	Right angle (degrees)
Measurement 1	32.918	41.477
Measurement 2	40.280	34.271
Measurement 3	37.674	37.101
Measurement 4	34.350	36.385
Measurement 5	32.021	42.745
Mean	**33.6**	38.4
Standard deviation	5.90	3.20

Measurement	Left angle (degrees)	Right angle (degrees)
Measurement 1	34.168	33.233
Measurement 2	35.002	35.379
Measurement 3	34.302	36.601
Measurement 4	34.651	35.359
Measurement 5	34.527	34.132
Mean	**34.5**	34.9
Standard deviation	0.29	1.16

Measurement	Left angle (degrees)	Right angle (degrees)
Measurement 1	42.314	43.587
Measurement 2	39.905	40.018
Measurement 3	40.613	40.492
Measurement 4	40.500	38.424
Measurement 5	41.017	39.663
Mean	**40.9**	40.4
Standard deviation	0.91	1.72

Measurement	Left angle (degrees)	Right angle (degrees)
Measurement 1	28.685	33.061
Measurement 2	27.746	32.149
Measurement 3	29.773	27.738
Measurement 4	29.807	27.532
Measurement 5	27.583	30.292
Mean	**28.7**	30.1
Standard deviation	0.95	2.24

Measurement	Left angle (degrees)	Right angle (degrees)
Measurement 1	24.596	31.831
Measurement 2	25.797	30.704
Measurement 3	24.769	32.189
Measurement 4	25.922	33.227
Measurement 5	27.150	34.663
Mean	**25.6**	32.5
Standard deviation	0.92	1.34

Measurement	Left angle (degrees)	Right angle (degrees)
Measurement 1	28.766	27.407
Measurement 2	26.994	31.358
Measurement 3	28.091	28.316
Measurement 4	24.547	28.589
Measurement 5	23.690	28.106
Mean	**26.4**	28.8
Standard deviation	1.98	1.36

A.2.2 Stainless steel

Measurement	Left angle (degrees)	Right angle (degrees)
Measurement 1	43.423	41.364
Measurement 2	42.794	41.609
Measurement 3	44.617	41.253
Measurement 4	43.639	42.403
Measurement 5	42.312	40.695
Mean	**43.4**	**41.5**
Standard deviation	0.79	0.56

Measurement	Left angle (degrees)	Right angle (degrees)
Measurement 1	29.072	28.583
Measurement 2	31.590	26.716
Measurement 3	28.133	28.982
Measurement 4	29.546	27.578
Measurement 5	31.254	26.459
Mean	**29.9**	**27.7**
Standard deviation	1.31	1.00

Measurement	Left angle (degrees)	Right angle (degrees)
Measurement 1	23.584	19.670
Measurement 2	23.661	18.780
Measurement 3	21.590	19.886
Measurement 4	22.521	20.784
Measurement 5	21.850	19.604
Mean	**22.6**	**19.7**
Standard deviation	0.86	0.64

Measurement	Left angle (degrees)	Right angle (degrees)
Measurement 1	24.252	26.635
Measurement 2	24.098	28.612
Measurement 3	23.583	26.854
Measurement 4	22.258	25.618
Measurement 5	24.410	27.259
Mean	**23.7**	**27.0**
Standard deviation	0.78	0.97

Measurement	Left angle (degrees)	Right angle (degrees)
Measurement 1	48.034	47.974
Measurement 2	47.454	46.411
Measurement 3	49.326	47.157
Measurement 4	48.772	46.413
Measurement 5	48.710	46.007
Mean	**48.5**	**46.8**
Standard deviation	0.65	0.70

Measurement	Left angle (degrees)	Right angle (degrees)
Measurement 1	22.736	25.804
Measurement 2	25.688	25.804
Measurement 3	23.294	24.473
Measurement 4	23.472	27.502
Measurement 5	23.164	26.073
Mean	**23.7**	**25.9**
Standard deviation	1.04	0.96

Measurement	Left angle (degrees)	Right angle (degrees)
Measurement 1	35.676	27.539
Measurement 2	36.545	24.321
Measurement 3	33.172	29.196
Measurement 4	36.566	25.590
Measurement 5	31.998	27.095
Mean	**34.8**	**26.7**
Standard deviation	1.87	1.67

Measurement	Left angle (degrees)	Right angle (degrees)
Measurement 1	27.533	22.504
Measurement 2	27.210	23.922
Measurement 3	22.042	22.699
Measurement 4	25.755	23.751
Measurement 5	27.055	23.520
Mean	**25.9**	**23.3**
Standard deviation	2.03	0.57

Measurement	Left angle (degrees)	Right angle (degrees)
Measurement 1	33.535	32.428
Measurement 2	37.169	29.277
Measurement 3	36.741	30.291
Measurement 4	32.688	28.367
Measurement 5	36.121	31.223
Mean	**35.3**	**30.3**
Standard deviation	1.80	1.43

A.2.3 Aluminum

Measurement	Left angle (degrees)	Right angle (degrees)
Measurement 1	83.273	89.613
Measurement 2	90.537	86.989
Measurement 3	87.910	89.950
Measurement 4	89.308	85.601
Measurement 5	93.890	88.794
Mean	**88.9**	88.2
Standard deviation	3.47	1.65

Measurement	Left angle (degrees)	Right angle (degrees)
Measurement 1	19.724	12.616
Measurement 2	18.533	17.464
Measurement 3	23.897	17.040
Measurement 4	21.407	18.198
Measurement 5	17.694	18.709
Mean	**20.3**	**16.8**
Standard deviation	2.21	2.17

Measurement	Left angle (degrees)	Right angle (degrees)
Measurement 1	33.129	26.293
Measurement 2	26.200	27.000
Measurement 3	32.604	32.780
Measurement 4	29.036	31.434
Measurement 5	26.293	30.300
Mean	**29.5**	**29.6**
Standard deviation	2.97	2.52

Measurement	Left angle (degrees)	Right angle (degrees)
Measurement 1	46.131	36.257
Measurement 2	46.962	34.121
Measurement 3	45.483	38.149
Measurement 4	44.916	38.269
Measurement 5	45.820	40.096
Mean	**45.9**	**37.4**
Standard deviation	0.68	2.03

Measurement	Left angle (degrees)	Right angle (degrees)
Measurement 1	28.098	24.060
Measurement 2	29.172	24.442
Measurement 3	27.786	29.159
Measurement 4	29.178	28.946
Measurement 5	26.075	29.308
Mean	**28.1**	**27.2**
Standard deviation	1.14	2.40

Measurement	Left angle (degrees)	Right angle (degrees)
Measurement 1	21.921	17.794
Measurement 2	21.353	19.176
Measurement 3	19.573	21.527
Measurement 4	22.327	20.425
Measurement 5	21.091	21.062
Mean	**21.3**	**20.0**
Standard deviation	0.95	1.36

Measurement	Left angle (degrees)	Right angle (degrees)
Measurement 1	30.484	29.617
Measurement 2	26.204	23.564
Measurement 3	30.043	25.473
Measurement 4	29.132	29.128
Measurement 5	27.115	29.602
Mean	**28.6**	**20.0**
Standard deviation	0.95	1.36

Measurement	Left angle (degrees)	Right angle (degrees)
Measurement 1	23.538	19.422
Measurement 2	22.559	18.699
Measurement 3	23.211	19.317
Measurement 4	22.587	19.250
Measurement 5	21.329	19.250
Mean	**23.65**	**19.19**
Standard deviation	0.78	0.25

A.2.4 Brass

Measurement	Left angle (degrees)	Right angle (degrees)
Measurement 1	83.273	89.613
Measurement 2	90.537	86.989
Measurement 3	87.910	89.950
Measurement 4	89.308	85.601
Measurement 5	93.890	88.794
Mean	**89.0**	**88.2**
Standard deviation	3.47	1.65

Measurement	Left angle (degrees)	Right angle (degrees)
Measurement 1	78.401	91.302
Measurement 2	69.533	90.928
Measurement 3	64.622	90.562
Measurement 4	66.647	88.787
Measurement 5	70.115	89.791
Mean	**69.9**	**90.3**
Standard deviation	4.71	0.90

Measurement	Left angle (degrees)	Right angle (degrees)
Measurement 1	79.102	64.453
Measurement 2	69.845	77.180
Measurement 3	83.925	84.297
Measurement 4	69.785	61.622
Measurement 5	70.733	71.312
Mean	**74.7**	**71.8**
Standard deviation	5.80	8.28

Measurement	Left angle (degrees)	Right angle (degrees)
Measurement 1	32.946	39.435
Measurement 2	31.952	33.433
Measurement 3	37.262	35.610
Measurement 4	29.033	35.566
Measurement 5	36.259	35.945
Mean	**33.5**	**36.0**
Standard deviation	2.98	1.94

Measurement	Left angle (degrees)	Right angle (degrees)
Measurement 1	25.598	24.238
Measurement 2	31.275	26.208
Measurement 3	32.779	23.570
Measurement 4	31.058	30.081
Measurement 5	34.969	23.600
Mean	**31.1**	**25.5**
Standard deviation	3.10	2.47

Measurement	Left angle (degrees)	Right angle (degrees)
Measurement 1	70.150	77.920
Measurement 2	70.977	78.574
Measurement 3	67.174	69.689
Measurement 4	67.552	72.906
Measurement 5	67.400	74.519
Mean	**68.7**	**77.2**
Standard deviation	1.59	2.89

Measurement	Left angle (degrees)	Right angle (degrees)
Measurement 1	71.251	69.232
Measurement 2	71.571	75.607
Measurement 3	72.242	71.695
Measurement 4	75.390	69.922
Measurement 5	75.586	71.582
Mean	**73.2**	**71.6**
Standard deviation	1.89	2.21

Measurement	Left angle (degrees)	Right angle (degrees)
Measurement 1	61.087	55.797
Measurement 2	60.825	53.750
Measurement 3	54.462	53.170
Measurement 4	56.540	57.792
Measurement 5	57.516	53.892
Mean	**58.1**	**54.9**
Standard deviation	2.54	1.70

Measurement	Left angle (degrees)	Right angle (degrees)
Measurement 1	105.700	109.792
Measurement 2	101.939	113.110
Measurement 3	104.673	109.373
Measurement 4	103.688	112.228
Measurement 5	106.348	111.854
Mean	**104**	**111**
Standard deviation	2.56	1.44

A.2.5 Epoxy

Measurement	Left angle (degrees)	Right angle (degrees)
Measurement 1	93.436	98.893
Measurement 2	97.988	100.549
Measurement 3	94.049	96.567
Measurement 4	94.623	96.967
Measurement 5	93.468	95.310
Mean	**95**	98
Standard deviation	2	2

Measurement	Left angle (degrees)	Right angle (degrees)
Measurement 1	89.710	93.256
Measurement 2	90.895	93.376
Measurement 3	90.856	101.579
Measurement 4	94.005	99.072
Measurement 5	93.698	96.528
Mean	**90**	97
Standard deviation	2	3

Measurement	Left angle (degrees)	Right angle (degrees)
Measurement 1	92.474	94.482
Measurement 2	91.986	99.196
Measurement 3	91.432	95.325
Measurement 4	90.121	96.247
Measurement 5	93.059	98.420
Mean	**92**	97
Standard deviation	1	2

Measurement	Left angle (degrees)	Right angle (degrees)
Measurement 1	93.064	97.779
Measurement 2	94.090	96.954
Measurement 3	92.554	95.207
Measurement 4	94.382	97.955
Measurement 5	97.249	95.984
Mean	**94**	97
Standard deviation	2	1

Measurement	Left angle (degrees)	Right angle (degrees)
Measurement 1	97.777	99.754
Measurement 2	99.556	99.734
Measurement 3	104.600	101.523
Measurement 4	99.474	101.629
Measurement 5	99.918	102.295
Mean	**100**	**101**
Standard deviation	2	1

Measurement	Left angle (degrees)	Right angle (degrees)
Measurement 1	96.418	103.738
Measurement 2	105.758	105.364
Measurement 3	102.727	106.348
Measurement 4	101.374	107.161
Measurement 5	100.823	105.901
Mean	**101**	**106**
Standard deviation	3	1

Measurement	Left angle (degrees)	Right angle (degrees)
Measurement 1	97.634	97.639
Measurement 2	100.225	97.184
Measurement 3	100.398	98.536
Measurement 4	95.202	98.574
Measurement 5	98.766	100.945
Mean	**98**	**99**
Standard deviation	2	1

Measurement	Left angle (degrees)	Right angle (degrees)
Measurement 1	105.632	101.218
Measurement 2	103.372	100.524
Measurement 3	103.522	101.485
Measurement 4	103.137	101.056
Measurement 5	105.480	101.129
Mean	**104**	**101.1**
Standard deviation	1	0.3

Measurement	Left angle (degrees)	Right angle (degrees)
Measurement 1	89.024	94.311
Measurement 2	88.661	91.841
Measurement 3	87.602	93.642
Measurement 4	90.341	91.210
Measurement 5	88.578	95.721
Mean	**88.8**	**93**
Standard deviation	0.9	2

Appendix B

Effect of flow

Surface												Mean
Glass	400	400	400	400	400	400	600	600	400	400	400	
	400	400	400									429 ± 70
Stainless steel	400	400	400	400	400	400	400	400	400	600	600	
	400	400										431 ± 72
Aluminum	400	600	400	400	600	400	400	600	600	400	600	
	600	600	400	400	400	400	400	600	400	600		500 ± 82
Brass	400	400	400	400	400	400	400	600	400	400	400	
	400	400	400	400	400	400	400					414 ± 45
Epoxy	200	200	0	200	200	200	0	200	200	400		
												180 ± 108

B.1 Detach of deposited droplet

Stirring rate needed to detach a deposited droplet of water with 15 wt% TBAB from different solid surfaces at ambient temperature.

Surface	Temp												Mean
Glass	$0-1°$	125	275	250	325	100	175	200	225	275	250	225	
		225	275	175	250	375	125	150					222 ± 17
Glass	$2-3°$	275	250	200	275	225	150	175	275	325	250	275	
		225	300	300	150	225	200						240 ± 51
Stainless steel	$3-4°$	200	100	125	100	100	125	225	175	100	100	125	
		125	175	150	150								138 ± 12
Aluminum	$0-1°$	150	350	200	150	150	125	125	100	100	100	125	
		100	250	200	150	175	125	125	100	125	100	100	147 ± 59
Brass	$2-3°$	100	100	100	100	125	125	100	125	125	100	100	
		125	125	125									112 ± 11
Epoxy	$0-1°$	200	100	100	150	100	150	150	150	150	150	100	
		100	150	100	100	100							128 ± 30

B.2 Detach of wet hydrate

Flow rate needed to detach a deposited wet hydrate particle of water with 15 wt% TBAB from different solid surfaces at ambient temperature.

Appendix C

Dynamic contact angles of droplets in a flow field

Dynamic contact angles of droplets of water with 15 wt% TBAB at different solid surfaces at ambient temperature

C.0.1 Glass

Measurement	Left angle (degrees)	Right angle (degrees)
Measurement 1	15.765	11.490
Measurement 2	12.980	12.953
Measurement 3	14.834	13.059
Measurement 4	12.845	12.377
Measurement 5	16.432	13.203
Mean	**14.6**	12.6
Standard deviation	0.65	0.28

Measurement	Left angle (degrees)	Right angle (degrees)
Measurement 1	15.215	14.415
Measurement 2	15.643	14.558
Measurement 3	15.899	11.842
Measurement 4	19.557	13.428
Measurement 5	16.016	13.764
Mean	**16.5**	13.6
Standard deviation	0.70	0.44

Measurement	Left angle (degrees)	Right angle (degrees)
Measurement 1	17.085	15.976
Measurement 2	15.638	15.807
Measurement 3	15.979	16.471
Measurement 4	17.881	13.644
Measurement 5	16.822	15.360
Mean	**16.7**	15.5
Standard deviation	0.36	0.44

Measurement	Left angle (degrees)	Right angle (degrees)
Measurement 1	19.831	14.786
Measurement 2	20.398	15.408
Measurement 3	18.323	15.216
Measurement 4	17.816	14.798
Measurement 5	18.751	16.413
Mean	**19.0**	15.3
Standard deviation	0.43	0.27

Measurement	Left angle (degrees)	Right angle (degrees)
Measurement 1	16.332	17.822
Measurement 2	15.421	19.798
Measurement 3	17.072	18.296
Measurement 4	14.472	16.434
Measurement 5	15.723	18.462
Mean	**15.8**	18.2
Standard deviation	0.39	0.49

C.0.2 Stainless steel

Measurement	Left angle (degrees)	Right angle (degrees)
Measurement 1	29.544	22.288
Measurement 2	33.524	21.255
Measurement 3	34.664	23.229
Measurement 4	30.205	23.621
Measurement 5	29.442	24.964
Mean	**31.5**	23.1
Standard deviation	0.98	0.56

Measurement	Left angle (degrees)	Right angle (degrees)
Measurement 1	64.012	28.057
Measurement 2	65.582	27.341
Measurement 3	65.076	29.668
Measurement 4	65.349	29.133
Measurement 5	64.750	27.449
Mean	**65.0**	28.3
Standard deviation	0.25	0.41

Measurement	Left angle (degrees)	Right angle (degrees)
Measurement 1	56.727	19.310
Measurement 2	53.937	22.619
Measurement 3	50.390	23.073
Measurement 4	52.938	22.919
Measurement 5	49.399	24.535
Mean	**52.7**	22.5
Standard deviation	1.17	0.77

Measurement	Left angle (degrees)	Right angle (degrees)
Measurement 1	57.250	32.174
Measurement 2	55.831	31.961
Measurement 3	52.196	29.780
Measurement 4	51.919	29.162
Measurement 5	51.983	31.671
Mean	**53.8**	31.0
Standard deviation	1.01	0.55

C.0.3 Alumnium

Measurement	Left angle (degrees)	Right angle (degrees)
Measurement 1	29.300	23.036
Measurement 2	26.858	22.549
Measurement 3	28.671	26.439
Measurement 4	28.700	26.220
Measurement 5	30.229	25.208
Mean	**28.8**	24.7
Standard deviation	0.49	0.72

Measurement	Left angle (degrees)	Right angle (degrees)
Measurement 1	64.295	30.146
Measurement 2	61.558	35.151
Measurement 3	56.996	29.403
Measurement 4	63.616	32.982
Measurement 5	59.446	33.957
Mean	**61.2**	32.3
Standard deviation	1.21	1.00

Measurement	Left angle (degrees)	Right angle (degrees)
Measurement 1	70.647	38.502
Measurement 2	68.492	36.651
Measurement 3	67.496	34.920
Measurement 4	67.496	33.755
Measurement 5	73.620	36.519
Mean	**69.6**	36.1
Standard deviation	1.05	0.72

C.0.4 Brass

Measurement	Left angle (degrees)	Right angle (degrees)
Measurement 1	32.507	41.345
Measurement 2	26.661	43.949
Measurement 3	27.878	45.012
Measurement 4	28.516	48.662
Measurement 5	29.846	44.220
Mean	**29.1**	45
Standard deviation	0.89	1.05

Measurement	Left angle (degrees)	Right angle (degrees)
Measurement 1	91.430	75.222
Measurement 2	93.902	75.667
Measurement 3	95.408	73.505
Measurement 4	93.787	77.413
Measurement 5	97.316	81.454
Mean	**94.4**	76.7
Standard deviation	0.97	1.21

Measurement	Left angle (degrees)	Right angle (degrees)
Measurement 1	94.958	83.023
Measurement 2	91.646	82.513
Measurement 3	94.371	81.392
Measurement 4	95.190	82.846
Measurement 5	93.289	80.022
Mean	**93.9**	82.0
Standard deviation	0.58	0.50

Measurement	Left angle (degrees)	Right angle (degrees)
Measurement 1	87.008	62.962
Measurement 2	73.446	61.250
Measurement 3	76.158	68.713
Measurement 4	80.943	68.632
Measurement 5	82.235	65.834
Mean	**80.0**	65.5
Standard deviation	2.12	1.34

C.0.5 Epoxy

Measurement	Left angle (degrees)	Right angle (degrees)
Measurement 1	86.026	68.444
Measurement 2	91.564	71.832
Measurement 3	93.549	67.252
Measurement 4	94.042	64.399
Measurement 5	96.497	63.571
Mean	**92.3**	67.1
Standard deviation	1.56	1.33

Measurement	Left angle (degrees)	Right angle (degrees)
Measurement 1	111.504	79.883
Measurement 2	104.036	79.726
Measurement 3	104.335	77.509
Measurement 4	106.499	79.516
Measurement 5	104.698	76.824
Mean	**106**	78.7
Standard deviation	1.24	0.57

Measurement	Left angle (degrees)	Right angle (degrees)
Measurement 1	92.725	76.400
Measurement 2	90.765	77.374
Measurement 3	86.031	82.428
Measurement 4	93.805	72.205
Measurement 5	90.165	69.928
Mean	**90.7**	75.7
Standard deviation	1.20	1.94

Measurement	Left angle (degrees)	Right angle (degrees)
Measurement 1	72.278	73.374
Measurement 2	72.432	75.041
Measurement 3	71.412	84.030
Measurement 4	75.538	80.538
Measurement 5	77.939	76.288
Mean	**73.9**	77.9
Standard deviation	1.10	1.74

Appendix D

Infrared Spectroscopy

An Infrared Spectroscopy Analysis was used to make sure the clay used to attach the plates in the container did not contaminate the petroleum ether.

D.1 Theory about Infrared Spectroscopy

Infrared radiation is the part of the electromagnetic spectrum with wavelengths longer than those associated with visible light (400-800nm), but shorter than microwaves (1nm). Almost any compound having covalent bonds, whether organic or inorganic, absorbs various frequencies of electromagnetic radiation in the infrared region.

Molecules can vibrate in two different ways: stretching and bending. Within these, there are different way to stretch or bend, for example symmetrical or asymmetrical. This makes a simple, linear molecule such as carbon dioxide, have four fundamental vibrations. Different groups of the molecule vibrates at different frequencies and the combinations of these vibrations is unique for this type of molecules [52]. An infrared spectroscopy reads these vibrations and can therefore to recognize the type of molecule, much as a fingerprint can be used for humans. It can also be used to determine structural information about a molecule [53]. By reading the number of signals, the position and height in the spectrum, the compound can be identified.

In this case, it was used to compare the spectra of a pure sample of petroleum ether against a sample that was possible contaminated by the clay.

An Infrared Spectroscopy is done/obtained by exposing a molecule to infrared radiation. The radiation is absorbed by the molecule and converted into energy of molecular vibration. When the radiant energy matches the energy of a specific molecular vibration, absorption occurs [52]. The changes in the light waves after they have passed through (or been absorbed) can be measured and gives an infrared adsorption pattern or infrared spectrum. (This spectra is then converted by a Fourier-transformation, from time to frequency.)

The radiation is given in terms of a unit called "wavenumbers [cm^{-1}]". The wavenum-

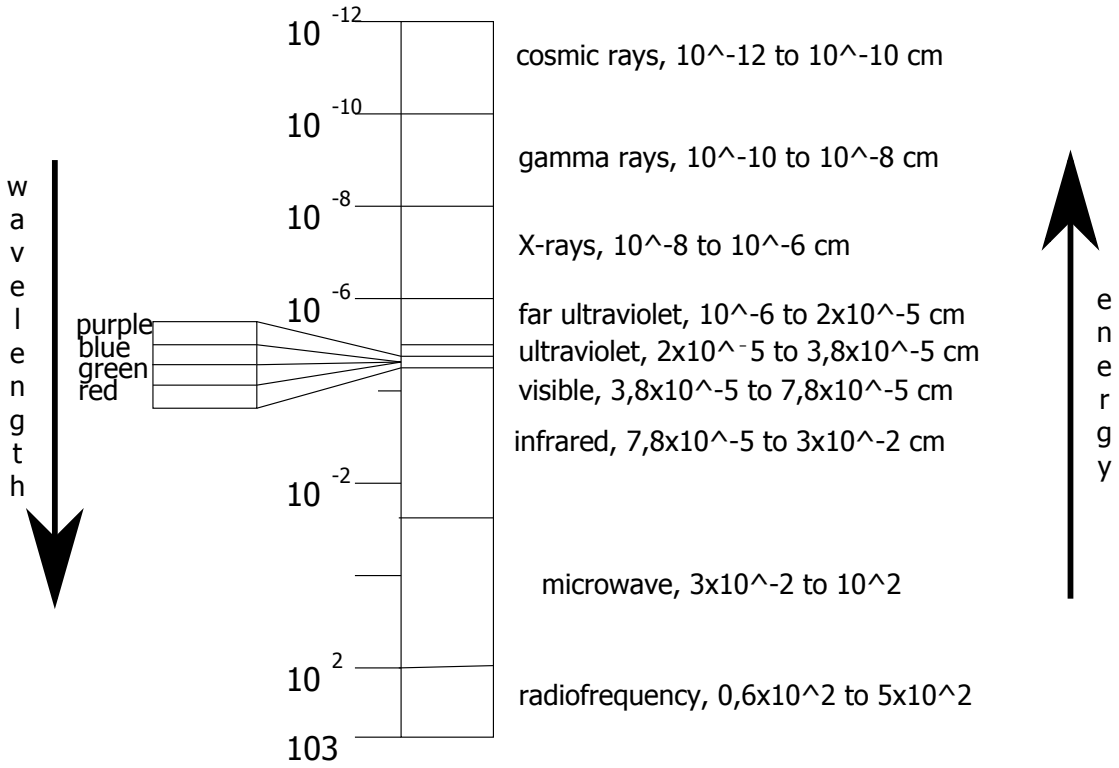

Figure D.1: A potion of the electromagnetic spectrum showing the wavelength of infrared radiation compared to other types of radiation. Picture redrawn from University of Colorado, Boulder's online theory for students [52].

ber number is simply

$$\overline{\nu}(cm^{-1}) = \frac{1}{\lambda(cm)} \tag{D.1}$$

where λ is the wavelength.

The frequency ν can be found from the wavenumber by multiplying it by the speed of light (expressed in centimeters per second):

$$\nu(Hz) = \overline{\nu}c = \frac{c(cm/sec)}{\lambda(cm)} \tag{D.2}$$

The main reason this is wavenumber is used as unit is that they are directly proportional to energy. A higher wavenumber corresponds to a higher energy.

D.2 Results from the Infrared Spectroscopy

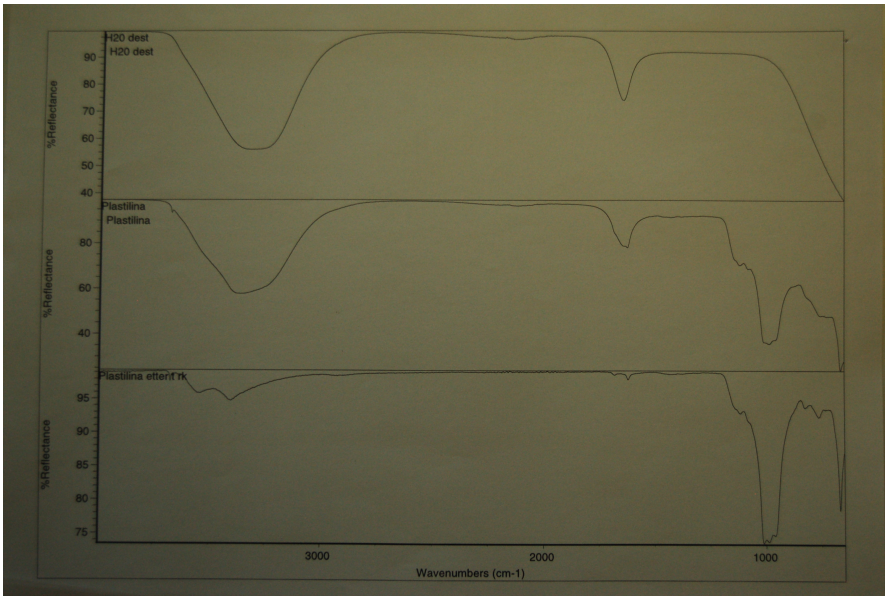

Figure D.2: The photo shows the print from the Infrared spectroscopy of distilled water, wet clay and dry clay, respectively. The depth (or height) of the peaks are different due to concentration. The number of peaks reflects the vibrations in the molecules. The peaks on the left hand side of the photo is hydrogen bonds, the peaks on the right hand side is only found for the clay, and is probably silica.

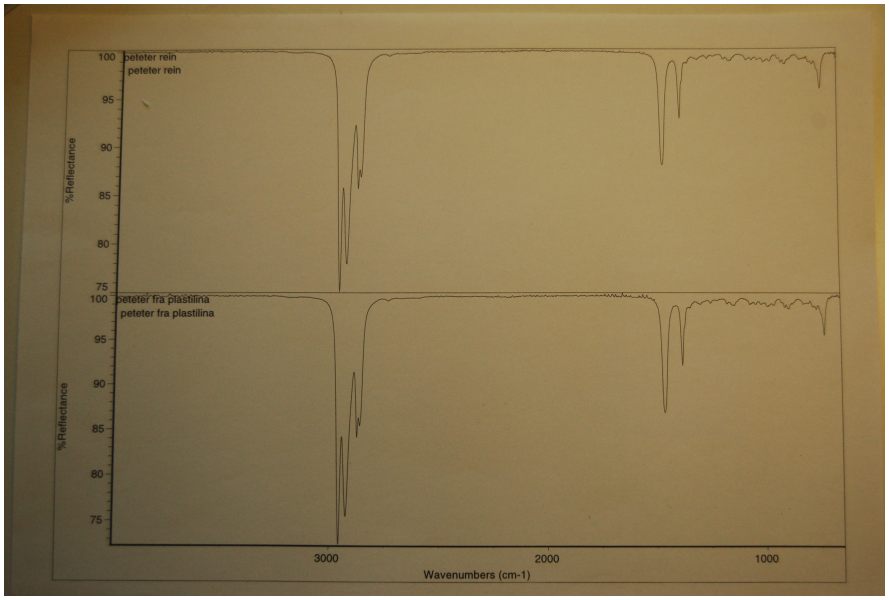

Figure D.3: The photo shows the spectroscopy of pure petroleum ether and petroleum ether with possible contamination from the clay. The number and distance between the peaks are the same, showing that the clay does not contaminate the petroleum ether. The difference in height is, as in picture D.2, due to difference in concentration. Another way to see that there is no contamination, is that the peaks at wavenumber $1000cm^{-1}$ which can be seen in D.2 and probably is silica, is not there.